

Fabrication techniques and morphological analysis of perovskite absorber layer for high-efficiency perovskite solar cell: A review

M.S. Jamal^{a,b}, M.S. Bashar^b, A.K. Mahmud Hasan^a, Zeyad A. Almutairi^{c,d}, Hamad F. Alharbi^c, Nabeel H. Alharthi^c, Mohammad R. Karim^e, H. Misran^f, Nowshad Amin^f, Kamaruzzaman Bin Sopian^a, Md. Akhtaruzzaman^{a,*}

^a Solar Energy Research Institute (SERI), Universiti Kebangsaan Malaysia (UKM), 43600 Bangi, Selangor, Malaysia

^b Institute of Fuel Research and Development, Bangladesh Council of Scientific and Industrial Research (BCSIR), Dhaka 1205, Bangladesh

^c Mechanical Engineering Department, King Saud University, P.O. Box 800, Riyadh 11421, Saudi Arabia

^d Sustainable Energy Technologies Center, King Saud University, Riyadh 11421, Saudi Arabia

^e Center of Excellence for Research in Engineering Materials, King Saud University, Riyadh 11421, Saudi Arabia

^f Institute of Sustainable Energy, Universiti Tenaga Nasional (The National Energy University), Jalan IKRAM-UNITEN, 43000 Kajang, Selangor, Malaysia

ARTICLE INFO

Keywords:

Anti-solvent
Crystallisation
Morphology
Perovskite solar cell, Power conversion efficiency
Stability

ABSTRACT

Organolead trihalide perovskite absorber layers are potential contenders in solar energy harvesting technologies because of their competitive lower fabrication cost, high power conversion efficiency, and ease of processing. The structural, interfacial and morphological properties are the key aspects to determine the stability and photon-to-current conversion efficiency of Perovskite solar cells (PSCs). Most contemporary research has emphasised on enhancing the power conversion efficiency (PCE) of perovskites by changing the fabrication process, solvent engineering, or precursor solution. With changes in these variables, the structure and morphology of perovskites also change, which affects the photon-to-current conversion efficiency and the stability of the PSCs. However, no stockpile records have aided in conducting corresponding research outcomes on this perspective. In this review, we summarise the effect of fabrication method on the structure and morphology, as well as the PCE and stability of PSCs. This review will help readers decipher the scientific and technological challenges concerning hybrid inorganic–organic PSCs.

1. Introduction

The conversion of solar radiation to electricity by a photovoltaic cell was first demonstrated in 1954. Due to the formation of a p–n barrier in silicon, photons were observed to generate electron–hole pairs which could be successfully transported to an external circuit [1]. Over the past five decades, silicon solar cells (SCs) have shown significant progress with high energy output and affordable production cost [2,3]. At present, the current global photovoltaic (PV) market is fully dominated by the crystalline silicon technology, in which 55% and 36% are polycrystalline and monocrystalline silicon modules, respectively. The remaining share of the PV market is open to the development of organic PVs (OPVs), perovskite solar cells (PSCs), dye-sensitised solar cells (DSSCs), quantum dot solar cells (QDSCs) and polycrystalline thin-film solar cells [4,5]. In comparison with other 1st generation SCs, Si-SCs have led to reduce cost with few limitations. Due to dependency on vacuum and temperature conditions during manufacturing, the

processing costs of these SCs are still high. Although the PV market is dominated by silicon-based solar cells, the price range of these solar cells remains below an affordable level for individual users due to their complex manufacturing process, high energy consumption, and high throughput cost [6–8]. The 3rd-generation SCs such as PSCs, OPVs, QDSCs, and DSSCs have offered a great versatility in terms of lighter weight, flexibility, choice of various synthesised material, simple device fabrication techniques, and most importantly, commercial-scale production with low cost [9–13]. Although the overall performance of 3rd-generation SCs has exhibited rapid evolution at the research scale, they lag behind other types of solar cells. Critical bottlenecks, such as limited efficiency, toxicity, and cost, and challenges with stability, reproducibility, and scalability hinder their ability to compete with existing solar technologies in power grid applications and the current electronics market. Considering the above-mentioned pros and cons, hybrid inorganic–organic PSCs are considered as one of the rising stars in the PV industry due to their high efficiency, low-temperature processing, and

* Corresponding author.

E-mail addresses: akhtar@ukm.edu.my, akhtar.brces@gmail.com (Md. Akhtaruzzaman).

<https://doi.org/10.1016/j.rser.2018.09.016>

Received 11 June 2018; Received in revised form 14 August 2018; Accepted 8 September 2018

Available online 06 October 2018

1364-0321/ © 2018 Elsevier Ltd. All rights reserved.

easy fabrication techniques.

Hybrid inorganic–organic perovskites indicate high absorption coefficients, high charge-carrier mobility, low exciton binding energy, long exciton diffusion length, and an easily tuneable band gap [14–19]. The staggering properties of the perovskite absorber have led to an increase in PCE from 3.8% to 22.1% within a period of only eight years [20,21]. However, PSCs are challenged with long-term stability and reproducibility problems, mainly due to the unstable behaviour of perovskite compounds in an ambient environment, and the synergistic factors of the functional components in PSCs [22]. Salhi et al. reviewed in depth the latest developments and shortcoming in the stability of PSCs. They presented moisture, elevated temperature, UV light, and exposure to the environmental condition as the leading causes of degradation in the PSCs [23]. Ansari et al. extensively reviewed the challenges and opportunities of perovskite solar cells. They focussed on the role of structure and composition of perovskite materials, and the deposition methods used for the perovskite layer [24]. Understanding the role of fabrication procedures in perovskite absorbers is important to further enhancing PV performance and reducing the overall production costs for role-to-role production. Low cost, easy reproduction, and facile deposition techniques are preferred for the fabrication of perovskite films. Various methods have already been subjected to intense investigation, and have been verified for the fabrication of high-quality perovskite layers for high-efficiency PSCs. Given that the film quality of perovskite plays a pivotal role in the overall performance of solar cells, obtaining high-quality perovskite films with high phase purity, fewer structural defects, suitable morphology, and high crystallinity are necessary.

In this review, we elaborate on the structure of perovskite materials and their development chronologically to the present day. The main part of this work discusses existing fabrication methods of perovskite film for PSCs applications. By considering the aforementioned technical and theoretical aspects, we discuss all existing fabrication methods of perovskite film with structural and morphological analysis for PSCs applications. Notably, the phase transition, microstructure, defect states, band gap, and optical properties of perovskite films are strongly affected by the post-operating temperatures and deposition methods. Moreover, the band gap, optical constant, and optical absorption may also be affected by processing techniques. Therefore, in this review, we focus on the correlation of the structural and morphological properties of perovskite films with their corresponding deposition techniques at the end of each section.

1.1. Structure and properties of perovskite compounds

Universally, the general chemical formula for perovskite material is AMX_3 . It consists of two different sizes of cations ('A' and 'M') and one anion ('X'), in which the ideal cubic symmetry of the 'M' cation is located in six-fold coordination while it is encircled by an octahedron of anions, while the 'A' cation is in a twelve-fold cuboid octahedral coordination, as shown in Fig. 1.

The most attractive features of perovskite structures are organic molecule cations that are based on amine ($CH_3NH_3^+$) at 'A' sites, metal cations (Ge^{2+} , Sn^{2+} and Pb^{2+}) at 'M' sites, and halide anions (Cl^- , Br^-

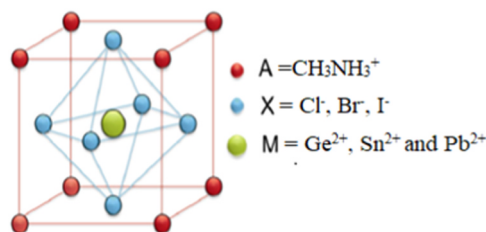


Fig. 1. Molecular structure of perovskite compound (Reprint permission from Ref. [25]).

Table 1

Effect of M cations on perovskite energy gap [32].

| Material | LUMO/eV | HOMO/eV | E_g /eV |
|-------------------------------|---------|---------|-----------|
| $CH_3NH_3PbI_3$ | – 3.88 | – 5.39 | 1.51 |
| $CH_3NH_3Sn_{0.3}Pb_{0.7}I_3$ | – 3.81 | – 5.12 | 1.31 |
| $CH_3NH_3Sn_{0.5}Pb_{0.5}I_3$ | – 3.67 | – 4.95 | 1.28 |
| $CH_3NH_3Sn_{0.7}Pb_{0.3}I_3$ | – 3.69 | – 4.92 | 1.23 |
| $CH_3NH_3Sn_{0.9}Pb_{0.1}I_3$ | – 3.57 | – 4.75 | 1.18 |
| $CH_3NH_3SnI_3$ | – 3.63 | – 4.73 | 1.10 |

and I^-) at 'X' sites. The extraordinary properties of this unique structure has led to significant interest among scientists worldwide [26]. In 1978, Weber synthesised the first organic–inorganic halide perovskite $CH_3NH_3PbX_3$ [27], which exhibited different colours when the stoichiometric parameter was varied. The ion 'A' balances the charge of the framework without distressing the band gap; however, the size may lead to shrinking or expansion of the crystal lattice and a final effect on the band gap [28–30]. A series of materials with different band gaps can be obtained by controlling the size of the 'A' ion. Metal–halide bond angle also indicates a significant effect on the band gap. The band gap of the metal halide increases with the decrease in bond angle. The band gap of various metal halides is shown in Table 1. Studies also show that the stability of the perovskite group follows the trend $AgI_3 < ASnI_3 < APbI_3$ [31].

Other mixed-lead halide perovskite compounds, such as $CH_3NH_3PbI_{3-x}Cl_x$, have direct band gaps in the range of 1.61–1.96 eV [33]. $CH_3NH_3PbI_{3-x}Br_x$ shows direct band gaps of 1.58–2.28 eV [30], which depend on the value of x. Therefore, these materials are excellent light absorbers that can effectively cover a wide range of solar emission spectra from ultraviolet to infrared wavelength regions. $CH_3NH_3PbI_3$ contains weak bond exciton binding energy ranging from 37 meV to 50 meV and provides a pathway for easy movement of free carriers [34–36]. It shows exceptional charge carrier transportation properties that make it a popular choice for optoelectronic device fabrication. As a single crystal, $CH_3NH_3PbI_3$ has large diffusion length that exceeds 175 μm , whereas in the form of thin film, $CH_3NH_3PbI_{3-x}Cl_x$ has a diffusion length of up to 1 μm , as presented in Table 2. Carrier mobility and recombination were measured for single crystals using Hall effect measurement and impedance spectroscopy, respectively, at 1 sun illumination. However, diffusion lengths of single crystals and thin films were measured by combining the mobility and lifetime. The Hall effect measurement was conducted with a sample size of 1.5 mm \times 1.5 mm \times 1 mm in dark conditions. All four electrodes were made of Ga. A source meter (Keithley 2400) was used to apply DC current, and a different source meter (Keithley 4200) was used to record the Hall voltage. The carrier recombination of thin film was measured by a laser flash spectrometer (LP920). The measurement was based on a standard transient absorption setup. During this observation, a nanosecond laser pulse is used to excite the sample. The time evolution of the differential absorption changes induced by the pump which is monitored by a continuous wave light source probe.

Fig. 2 provides the electronic band structure of AMX_3 perovskite ($A = CH_3NH_3$, CH_2NHCH_2 , Cs; $M = Pb$, Sn; $X = I$, Br, Cl) with several crystal structures. In Fig. 2(a)–(d), the band gaps increase with increasing electronegativity of M–site and X–sites, and decreasing symmetry of the crystal structures (orthorhombic > tetragonal > cubic). However, there is no existing mechanism to explain the change in band gap with the variation in the A cation [37].

1.2. Chronological development of PSCs

The chronological development of PSCs is shown in Table 3. In 2009, Miyasaka first introduced PSCs with mesoporous TiO_2 as the template for $CH_3NH_3PbI_3$ and $CH_3NH_3PbBr_3$ as a photoactive layer, which resulted in a PCE of 3.81% [21]. Park et al. optimised a method

Table 2
Charge carrier properties of organic-inorganic lead halide perovskite.

| Perovskite Compound | Carrier Mobility ($\text{cm}^2 \text{V}^{-1} \text{s}^{-1}$) | Carrier Recombination (μs) | Diffusion Length, L_D (μm) | Refs. |
|---|--|---|---|---------------------|
| $\text{CH}_3\text{NH}_3\text{PbI}_3^{\text{SC}}$ | 24.8 ± 4.1 | 95 | ~ 175 | Dong et al. [38] |
| $\text{CH}_3\text{NH}_3\text{PbBr}_3^{\text{SC}}$ | 2.5 | 0.357 | $\sim 0.3\text{--}1.7$ | Shi et al. [39] |
| $\text{CH}_3\text{NH}_3\text{PbI}_3^{\text{TF}}$ | – | 0.0096 | 0.129 ± 41 | Stranks et al. [40] |
| $\text{CH}_3\text{NH}_3\text{PbI}_{3-x}\text{Cl}_x^{\text{TF}}$ | – | 0.2727 | 1.069 ± 0.204 | Stranks et al. [40] |

^{SC} Single Crystal, ^{TF} Thin film.

of depositing electrolytes in perovskite formulation with an increased PCE of up to 6.5% [41]. Subsequently, in 2012, two groups led by Grätzel and Park, and Snaith et al. reported major breakthroughs in PSC technology, thereby providing insight on the potential use of PSCs. Park and Grätzel replaced the liquid electrolyte with Spiro-OMeTAD as an HTM and fabricated an all-solid-state PSCs, which achieved 9.7% efficiency [42]. Snaith and co-worker reported the mesoporous (mp) framework of alumina (Al_2O_3) instead of the mp- TiO_2 on TiO_2 compact layer (FTO/Compact TiO_2 /Mesoporous Al_2O_3 or mesoporous TiO_2 / $\text{CH}_3\text{NH}_3\text{PbI}_2\text{Cl}$ /Spiro-OMeTAD/Ag) which further increased the PCE to 10.9% by using a mixed halide $\text{CH}_3\text{NH}_3\text{PbI}_{3-x}\text{Cl}_x$ absorber [43]. Incorporation of a mesoporous Al_2O_3 insulator along with compact TiO_2 obstructed any formation of near-band-gap density of states compared

to mp- TiO_2 -based PSCs. This phenomenon contributed to the transportation of electrons within the perovskite, and increased the open-circuit voltage (V_{oc}) up to 1.12 V. However, Al_2O_3 possesses an unfavourable electronic energy level due to the band alignment mismatch for electron transfer to Electron transport layer (ETL) from perovskite layer. The conduction band (CB) edge of alumina (~ -2.1 eV) [44] is greater than the CB-edge of Perovskite (-3.9 eV), confirming that the electron tends to remain within perovskite rather than being transported to n-type TiO_2 [45]. At the end of 2012, Grätzel et al. proposed a hole conductor-free mesoscopic-PSC, which recommended that the perovskite compound itself could facilitate as hole conductor in PSCs [46]. In 2013, numerous fabrication techniques for perovskite absorber materials were reported in mesoporous and planar structures

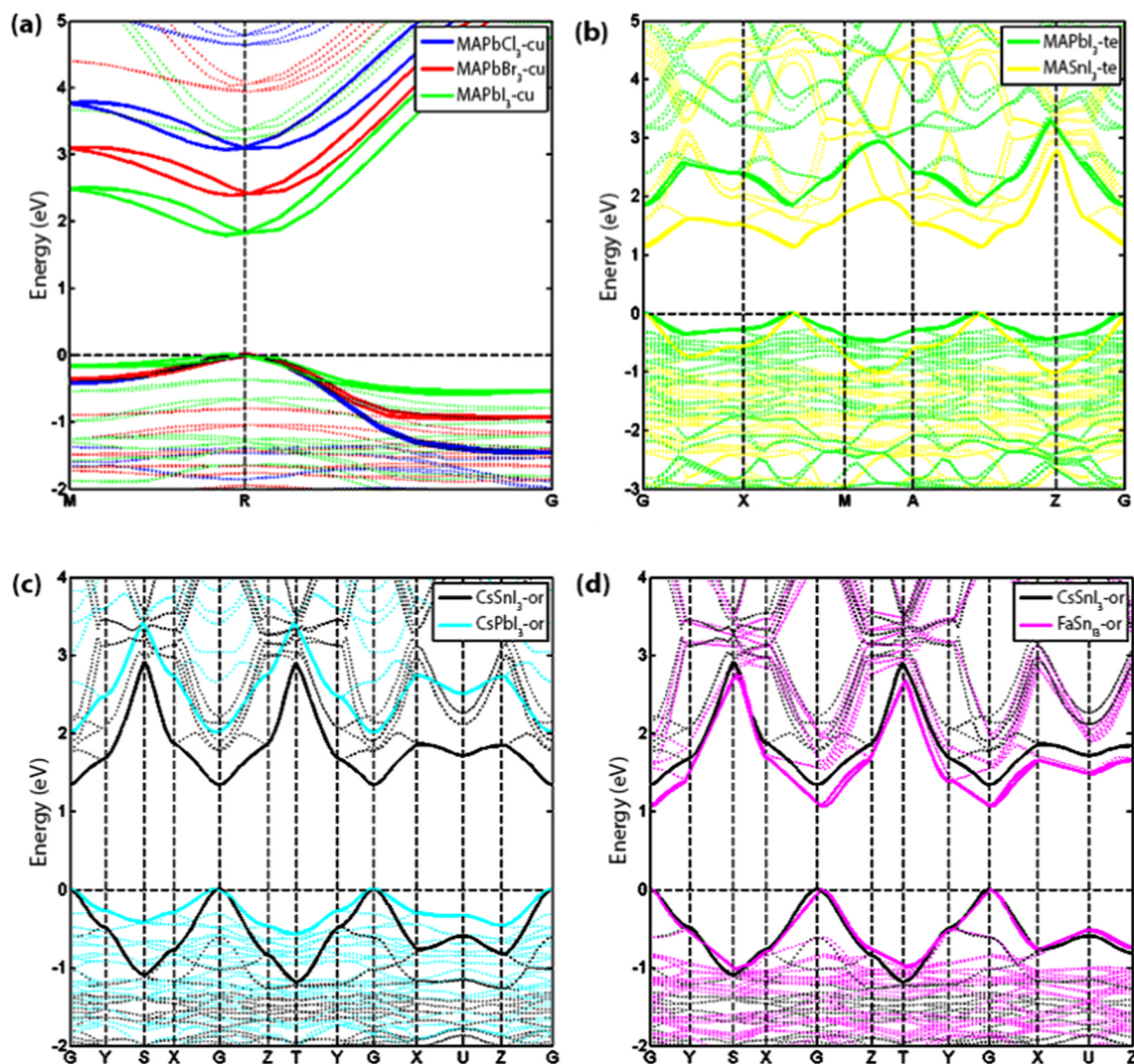


Fig. 2. Calculated band structure for (a) pseudo-cubic structure of $\text{CH}_3\text{NH}_3\text{PbX}_3$ ($X = \text{I}, \text{Br}, \text{Cl}$) (b) tetragonal structure of $\text{CH}_3\text{NH}_3\text{MI}_3$ ($M = \text{Sn}, \text{Pb}$), (c) orthorhombic structure CsMI_3 ($M = \text{Sn}, \text{Pb}$) (d) orthorhombic structure of ASnI_3 ($A = \text{Cs}, \text{CH}_2\text{NHCH}_2$) (Reprint permission from Ref. [37]).

Table 3
Chronological development of perovskite solar cells.

| Year | Device Structure | Structure | Efficiency (%) | Refs. |
|------|--|-----------|----------------|----------------------|
| 2009 | TiO ₂ /CH ₃ NH ₃ PbI ₃ /Liquid electrolyte | – | 3.81% | Kojima et al. [21] |
| 2011 | cl-TiO ₂ /CH ₃ NH ₃ PbI ₃ QD /Liquid electrolyte | – | 6.5% | Im et al. [41] |
| 2012 | cl-TiO ₂ /mesoporous TiO ₂ /CH ₃ NH ₃ PbI ₃ /Spiro-MeOTAD | mp | 9.7% | Kim et al. [57] |
| | cl-TiO ₂ /mesoporous Al ₂ O ₃ /CH ₃ NH ₃ PbI ₂ Cl/Spiro-OMeTAD | mp | 10.9% | Lee et al. [43] |
| 2013 | cl TiO ₂ /CH ₃ NH ₃ PbI _{3-x} Cl _x /Spiro- OMeTAD | n-i-p | 15.4% | Liu et al. [17] |
| | TiO ₂ /CH ₃ NH ₃ PbI _{3-x} Cl _x /Spiro-OMeTAD | n-i-p | 15.0% | Burschka et al. [19] |
| 2014 | NiMgLiO/MAPI ₃ /Ti(Nb)O _x | p-i-n | 15.6% | Chen et al. [58] |
| | Yttrium-doped TiO ₂ /Perovskite/Spiro-OMeTAD | n-i-p | 19.3% | Zhou et al. [49] |
| 2015 | ITO/PEDOT:PSS/CH ₃ NH ₃ PbI ₃ (MAPbI ₃)/PCBM | p-i-n | 18.1% | Heo [59] |
| | bl-TiO ₂ / mp-TiO ₂ /(FAPbI ₃) _{1-x} (MAPbBr ₃) _x /PTAA | mp | 20.1% | Yang et al. [50] |
| 2016 | NiMgLiO/FA _{0.85} MA _{0.15} Pb(I _{0.85} Br _{0.15}) ₃ /PCBM/ Ti(Nb)O _x | p-i-n | 18.2% | Wu et al.[60] |
| | cl-TiO ₂ /mp-TiO ₂ /FA _{0.81} MA _{0.15} PbI _{2.51} Br _{0.45} /Spiro-OMeTAD | mp | 19.6% | Li et al. [61] |
| 2017 | FTO/thin-barrier TiO ₂ /mp-TiO ₂ /perovskite composite layer/perovskite upper layer/PTAA/Au | mp | 22.1% | Yang et al. [20] |

[17,19,47]. Grätzel et al. again reported the sequential deposition technique, in which PbI₂ crystals were first spin-coated and annealed on top of mp-TiO₂ before consecutive dipping in methylammonium iodide (MAI) solution, and showed a PCE up to 15% for mp-PSCs [19], whereas inverted mp-PSCs with FTO/NiO/meso-Al₂O₃/CH₃NH₃PbI₃/PCBM/BCP/Ag were reported to show a 13% PCE via two-step deposition [48]. Snaith et al. fabricated a simple planar heterojunction (PHJ) PSC on a compact layer of TiO₂ by a vapour-deposition method, thereby producing a PCE of ~ 15.4% [17]. Seok et al. reported on mp-PSCs with 16.4% efficiency by drop-casting toluene during spin coating of perovskite precursors dissolved in a mixed solvent of dimethylsulfoxide (DMSO) and γ -butyrolactone (GBL) [31]. By optimising the perovskite deposition method, and using Yttrium-doped TiO₂ as the ETL, Yang and his team further managed to enhance PCE (19.3%) [49]. Record-breaking PSC performance with PCE > 20% by using formamidinium iodide and dimethylsulphoxide (DMSO) intercalation in PbI₂ with mp-PSCs structure was verified for the first time [50]. In 2016, Grätzel et al. reported a cation engineering method with the incorporation of inorganic caesium for triple cation perovskite Cs_x(MA_{0.17}FA_{0.83})_(100-x)Pb(I_{0.83}Br_{0.17})₃ in mp-PSCs, which achieved approximately 21.1% PCE with stability for about 250 h. During the transformation from FAPbI₃ to a mixed (α or β) CsFA_{1-x}PbI₃ system upon incorporation of Cs, there may be reduction in entropy of approximately 200–300 K, resulting in a lessening of free energy within the triple cation perovskite. The reduction in free energy may justify the perceived favourability in elevating stability at lower temperatures for mixed cation perovskites [51]. The incorporation of Rb cations in RbCsMAFA PSC devices with mp-PSCs maintained stability for 500 h. RbCsMAFA has less ionic defects as compared to CsMAFA. Ionic defects within the RbCsMAFA lattice are less likely to migrate. Both are highly desired to increase the device performance and long-term stability [52]. Despite the majority of the record-breaking PSCs appearing in mp-PSCs with TiO₂ as the mesoporous template, the inverted structure of PSCs in planar configuration also indicates stable performance [53–56].

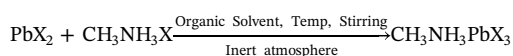
2. Deposition methods of perovskite films: structural and morphological analysis

Fabrication methods are broadly classified as (A) wet chemistry processing, and (B) vapour assisted processing. Wet processing methods include the one-step deposition (OSD) method, and sequential deposition method (SDM), and vapour-assisted processes are comprised of the vapour-assisted solution process (VASP), chemical vapour deposition (CVD), thermal vapour deposition (TVD) method, and microwave irradiation process (MIP). Here, we focus on the correlation of the structural and morphological properties of perovskite films with their corresponding deposition techniques.

2.1. Wet chemistry processing

2.1.1. OSD method

The first PSCs were developed by Kojima et al. in 2009 [21] where they followed Kitazawa's method of fabricating a perovskite absorber layer, and investigated the optical properties of methylammonium lead iodide to produce mixed halide or iodide only [62]. In this method, the stoichiometric composition of organic halides (CH₃NH₃X) and lead halides (PbX₂) were dissolved in GBL, dimethylformamide (DMF), or DMSO inside a nitrogen glove box to prepare a methylammonium lead halide (CH₃NH₃PbX₃) solution, shown as follows.



The CH₃NH₃PbX₃ film was deposited by spin coating of the CH₃NH₃PbX₃ precursor on top of the TiO₂ layer. At first, the precursor was spin-coated at a low spinning rate, and after a few seconds, the spinning rate gradually increased to produce a dense layer of CH₃NH₃PbX₃. Once the coating process was finished, the perovskite films were annealed [63]. A schematic of the OSD technique for the perovskite absorber layer is shown in Fig. 3.

Single-halide (CH₃NH₃PbI₃) and mixed-halide (CH₃NH₃PbCl_{1-x}I_x) perovskite compound have been extensively applied to harvest light in PSCs [64]. Mixed halide shows superior PV performance, such as high charge carrier mobility, large exciton diffusion length, and small exciton binding energy [40] compared with other cell structures. The OSD method gained popularity for its one-step simple fabrication, which leads to slow crystallisation. The resultant CH₃NH₃PbX₃ films shows high-density defects that result in limited performance for PSCs [25]. This deposition technique indicates that the quality of perovskite film mainly depends on the deposition conditions, such as annealing temperature, atmosphere environment, substrate materials, and film thickness [65]. To obtain a desirable film quality, uniformity of film thickness and morphology control are crucial parameters in the OSD method. Another challenge of the OSD method is reducing the pinholes in the perovskite film. To overcome all aforementioned issues in OSD, the anti-solvent dripping (ASD) method is introduced to regulate the kinetics of crystal growth and film quality [31]. A simple representation

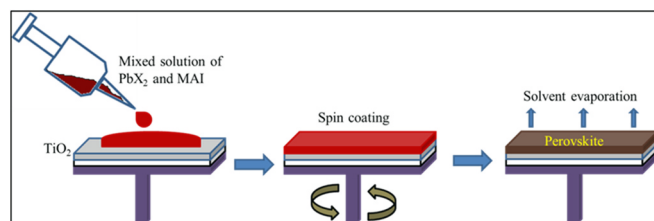


Fig. 3. Schematic illustration obtaining perovskite layer by one step deposition (OSD) method.

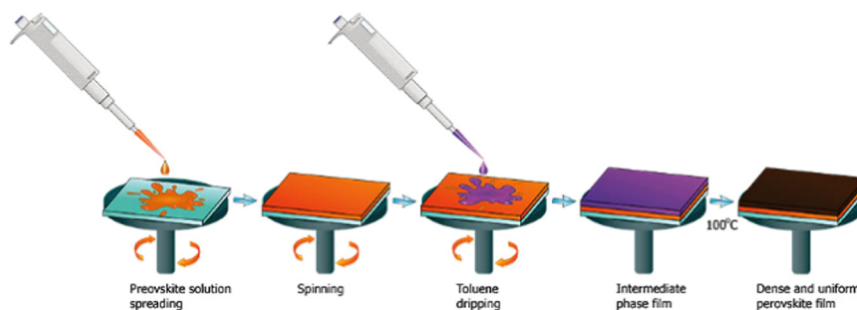


Fig. 4. Simple representation of anti-solvent treatment for the OSD technique.

of anti-solvent treatment for the OSD technique is shown in Fig. 4.

In the ASD method, the precursor of perovskite solution is dissolved into a DMSO and GBL mixed solution. Then the perovskite was formed on the substrate by spin coating. A certain amount of anti-solvent is dripped during spin coating and the substrate is annealed at 100 °C, which results in a uniform and smooth perovskite film with large grains [66]. A significant increase of PCE is observed due to the enhancement of surface morphology of perovskite film.

A comparative analysis of the $\text{CH}_3\text{NH}_3\text{PbI}_3$ absorber in OSD and ASD is shown in Fig. 5. Fig. 5(a) and (b) show the surface morphology of mesoporous TiO_2 and the OSD of $\text{CH}_3\text{NH}_3\text{PbI}_3$ on the top surface of the mp- TiO_2 layer, respectively. In Fig. 5(b), island-like non-uniform $\text{CH}_3\text{NH}_3\text{PbI}_3$ crystals on top of the mp- TiO_2 layer can be observed, which may be attributed to the wettability and presence of two cations on the coating solution [67]. Upon successful ASD treatment, a dense layer of larger grain size (100–500 nm) $\text{CH}_3\text{NH}_3\text{PbI}_3$ crystals are observed as shown in Fig. 5(c). This significant formation of $\text{CH}_3\text{NH}_3\text{PbI}_3$ crystals by the ASD method has boosted perovskite research to an entirely new dimension.

Different anti-solvents, such as $\text{C}_6\text{H}_5\text{Cl}$, C_6H_6 , $\text{C}_6\text{H}_5(\text{CH}_3)_2$, $\text{C}_6\text{H}_5\text{CH}_3$, CH_3OH , $\text{C}_2\text{H}_5\text{OH}$, $\text{C}_2\text{H}_6\text{O}_2$, $(\text{CH}_3)_2\text{CHOH}$, CHCl_3 , $(\text{CH}_2)_3\text{CH}_2\text{O}$, CH_3CN and $\text{C}_6\text{H}_5(\text{CN})$ have been used for the preparation of high-quality Pb-based perovskite crystalline films [17,18,69,70]. Scanning electron microscopy (SEM) reveals outstandingly different surface morphologies of MAPbI_3 film formed by different anti-solvents,

as shown in Fig. 6. The surface morphology of the MAPbI_3 film is significantly changed by the ASD method. Many voids and pinholes are observed during the deposition perovskite layer by OSD method. By contrast, the smooth and homogeneous surface morphology from the anti-solvent process unveils pinholes with large MAPbI_3 crystals which are densely packed. Average particle sizes are 158, 148, 87, 195, and 288 nm for MAPbI_3 films treated with toluene, chlorobenzene, chloroform, diethyl ether, and diisopropyl ether, respectively [71]. The large crystallite size of MAPbI_3 is obtained treating by diisopropyl ether compared to films prepared by other solvents, such as $\text{C}_6\text{H}_5\text{Cl}$, $\text{C}_6\text{H}_5\text{CH}_3$, CHCl_3 , or $(\text{C}_2\text{H}_5)_2\text{O}$. A better quality and entire surface coverage of MAPbI_3 film substantially enhances PSCs performance and improves the continued reproducibility of PSCs.

Xiao et al. first fabricated compact perovskite films with full surface coverage by using a fast deposition–crystallisation method. They manage to get complete surface coverage perovskite layer. Chlorobenzene as an anti-solvent is dripped after the initial few seconds of spin coating of a perovskite precursor and obtained a PCE of 13.0% under 1.0 sun illumination conditions [70]. The purpose of using anti-solvent was to rapidly reduce the solubility of $\text{CH}_3\text{NH}_3\text{PbI}_3$ quickly in the DMF and DMSO mixed solvent, and promoting fast nucleation and formation of $\text{CH}_3\text{NH}_3\text{PbI}_3$ crystals in the film. The film morphology was highly uniform over the entire substrate for $\text{C}_6\text{H}_5\text{Cl}$, C_6H_6 , $\text{C}_6\text{H}_5(\text{CH}_3)_2$ and $\text{C}_6\text{H}_5\text{CH}_3$ anti-solvents. However, the non-uniformity was observed in the central area of the perovskite films while using different anti-

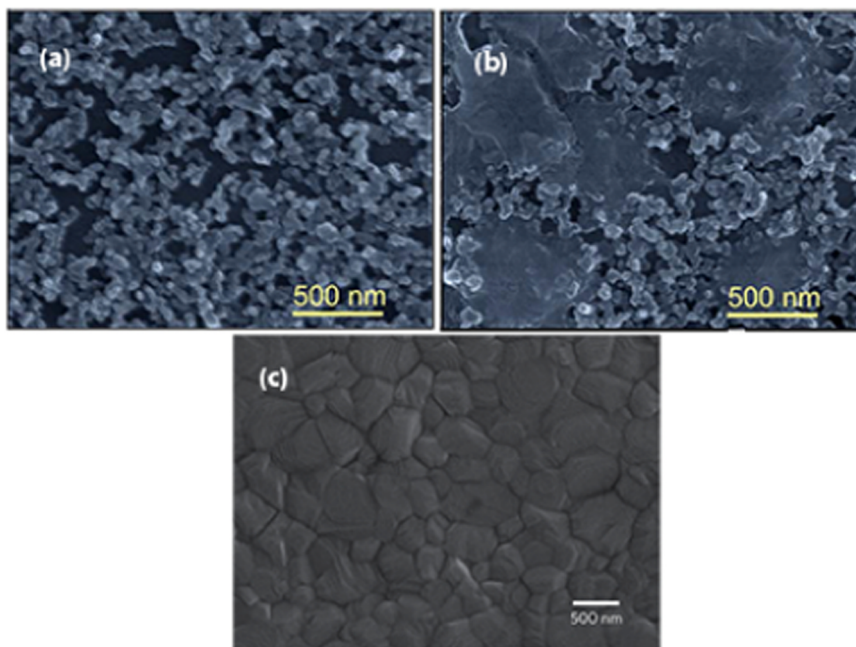


Fig. 5. SEM micrograph of (a) mesoporous TiO_2 (b) one-step deposition of MAPbI_3 on top of mp- TiO_2 layer (Reprint permission from Ref. [68]) (c) morphology of MAPbI_3 by anti-solvent (toluene) treatment for OSD method (Reprint permission from Ref. [31]).

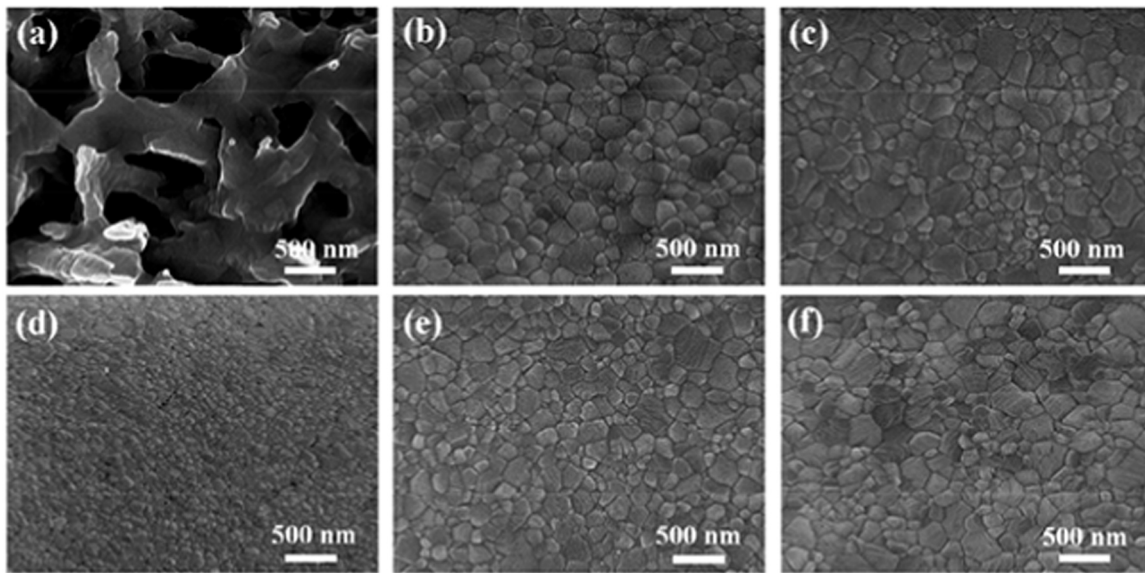


Fig. 6. SEM micrograph of perovskite films prepared by using different anti-solvents: (a) without anti-solvent (b) $C_6H_5CH_3$ (c) C_6H_5Cl (d) $CHCl_3$ (e) diethyl ether, and (f) di-isopropyl ether (Reprint permission from Ref. [71]).

solvents [72]. In 2016, Son et al. fabricated high-performance $CH_3NH_3PbI_3$ film by using diethyl ether as an anti-solvent, and improved PCE up to 20.1% for over 50 cells. They reduced the current-voltage hysteresis behaviour by using grain boundary healing process [69]. Jeon et al. fabricated highly uniform and thick perovskite absorber layer by toluene drop casting method using a mixture solvent of GBL and DMSO. In this process, they achieved certified PCE of 16.2% without hysteresis [31]. The addition of $MAPbBr_3$ into $FAPbI_3$ stabilised perovskite phase of $FAPbI_3$ with toluene as the anti-solvent agent, thereby improving the PCE of the PSC by more than 18% [18]. In 2017, Yang et al. showed that the concentration of defect states reduced the overall PSC performance. They showed that the concentration of deep-level defects could be reduced by ASD treatment. By adding excess triiodide ions into precursor solution achieved a certified PCE 22.1% and 19.7% for small cells and in 1 cm cells, respectively [20].

To enhance the morphology, stability, and excitonic and optoelectronic properties of hybrid inorganic–organic perovskite film, the addition of favourable additives have facilitated perovskite crystal growth. Various polymers, metal halide salts, organic halide salts, polymer, fullerene, nanoparticles, and inorganic acids are the additives most widely used to enhance the morphology of thin-film perovskites [73]. Polymers indicate a significant influence as additives to enhance uniform crystallisation, optimise the kinetics of crystal growth, and improve device performance. Polyethylene glycol (PEG) [74,75], amine-polymer poly[(9,9-bis(3'-(N,N-dimethylamino) propyl)-2,7-fluorene)-alt-2,7-(9,9-dioctylfluorene)] [76], polyvinylpyrrolidone [77], and polyacrylonitrile [78] are the most commonly used polymer additives for PSCs. Poor morphology control and surface coverage of the $CH_3NH_3PbI_{3-x}Cl_x$ film on TiO_2 are common problems for PSCs. Su et al. first solved this problem by using polyethylene glycol (PEG) as an additive in a $CH_3NH_3PbI_3$ precursor during the fabrication process, and successfully enhanced PCE ~ 25% more by adding 1 wt% of PEG. The SEM micrograph in Fig. 7 shows the change in surface coverage and morphology of $CH_3NH_3PbI_3$ layer from changing the amount of PEG. In the case of pristine perovskite film, crystals grow and aggregate in the large domain with poor coverage (86.44%), whereas 1 wt% PEG added to perovskite film decreases the size of the domain and void, and increases the coverage area (98.13%). However, an interesting feature is that the size and amount of crystal and void continuously increase with the amount of PEG added [74].

Alkali metal halide salts, such as NaI, CuI, CuBr, AgI [79], NaCl, and

KCl [80], are used as additives in the $CH_3NH_3PbI_3$ precursor during PSC fabrication which aids in enhancement of crystal growth of PbI_2 films by chelating with Pb^{2+} ions. As a result nanostructured morphologies of PbI_2 film is observed. These films of PbI_2 promote homogeneous nucleation and large crystal sizes, which enhance the morphology and crystalline properties of $CH_3NH_3PbI_3$ films. The aforementioned metal halides influence recrystallization of small grains, passivate grain boundaries and interfacial states, thereby permitting for efficient electron-hole pair generation and dissociation in $CH_3NH_3PbI_3$ films. Photoluminescence (PL) intensity measurements indicate that $CH_3NH_3PbI_3$ films prepared with salt additives feature a small number of recombination. The PCE is enhanced by 33% upon incorporation a small amount of alkyl halide. Moreover, the device stability is increased with only 16.5% degradation over 50 days compared to device prepared without the additive.

Han et al. explored a route to control and improve perovskite crystallisation by using methyl ammonium acetate (MAAc) and thiosemicarbazide (TSC) with molar ratios of 10–15% and 3–5%, respectively. Introducing MAAc in the precursor solution aids in generating a highly uniform $MAPbI_3$ film with full coverage morphology using the OSD method; however, a small amount of TSC efficiently improves the perovskite crystal size, as shown in Fig. 8. A combination of MAAc and TSC aids in uniform perovskite film formation with large grain size, low-density defects, and an ultra-smooth surface and enhances the PCE as well as stability of PSCs. The highest PCE (19.19%) for inverted planar PSCs has been achieved by widely-used $MAPbI_3$. Interestingly, the PSCs retain over 80% of the initial efficiency after 42 days of continuous illumination or 20 days of thermal aging at 80 °C [81].

2.1.2. Two-step deposition

2.1.2.1. SDM. In 2013, Burschka et al. first introduced the SDM to fabricate a perovskite layer that considerably changed the PCE and resulted in a PCE of more than 15%. In this process, they succeed to fabricate highly efficient perovskite layer by the SDM [19,50,82]. One of the key advantages of the SDM is the uniform and smooth surface of the perovskite layer. A schematic of the SDM is shown in Fig. 9. In this method, a PbI_2 layer is spin-coated over the top of the substrate and then dried before being dipped into the MAI-isopropyl alcohol solution for full conversion to $MAPbI_3$.

Dipping the TiO_2/PbI_2 composite film into a CH_3NH_3I solution in 2-propanol changes the substrate's colour instantly from yellow to dark

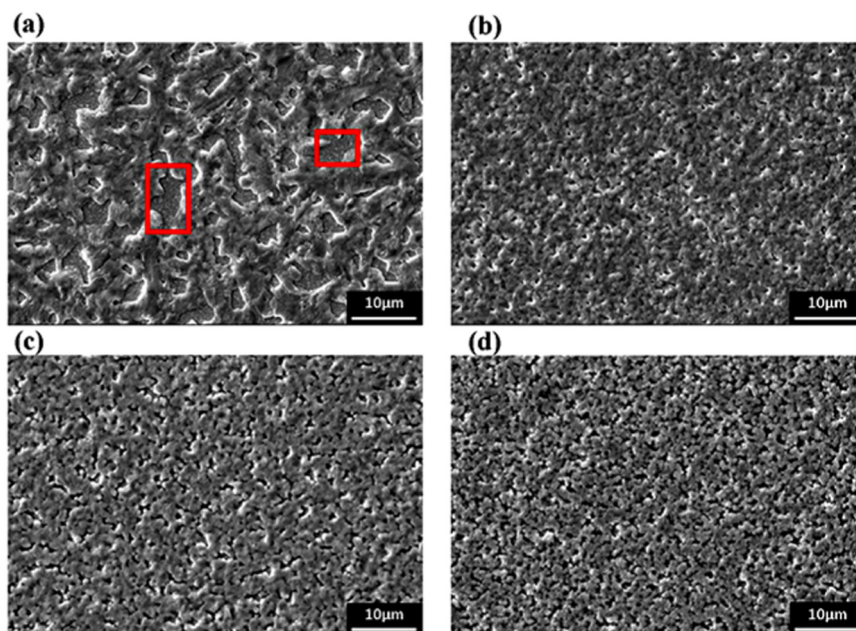


Fig. 7. SEM micrograph of perovskite film with (a) no PEG (pristine) (b) 1 wt% PEG (c) 2 wt% PEG, and (c) 3 wt% PEG as additives on the top of the TiO₂ layer (Reprint permission from Ref. [74]).

brown, which indicates the formation of CH₃NH₃PbI₃ [19]. This method allows for the PbI₂ crystallites to be confined to a small size, which subsequently increases their rate of conversion to CH₃NH₃PbI₃. In the dipping process, the physical and optoelectronic properties of the MAPbI₃ depend on the reaction time and solution concentration. A similar experiment was conducted for mp-TiO₂ substrates; however, better efficiency was obtained by slight modification of this method by pre-wetting the PbI₂ film by dipping it in iso-propanol for 1 s before dipped into the MAI solution. The SDM process exhibited 14.1% certified PCE. Using this approach, the morphology could be easily controlled with reduced defects and surface roughness of the perovskite film by controlling the concentration of the MAX solution. The SDM decreases the surface roughness and improves the pore filling of the perovskite absorber layer [68]. A few researchers [83,84] have reported that the formation of pinholes cannot be prevented in solution-processed film due to its natural mechanism [85] and a special separate treatment is needed to reduce pinhole formation. The imbalance of grain sizes and surface smoothness is one of the shortcomings of SDM, because surface smoothness decreases with the increase in grain size. Another drawback is the incomplete conversion of the perovskite compound. When PbI₂ film is dipped into the MAI solution, lead halide readily reacts with the small surface molecules and forms a dense layer that impedes the penetration of MAI into the underlying layer; however, this issue is addressed by advanced device engineering [5].

In SDM, concentrations of MAI and PbI₂ have a great impact on the

morphology and electronic properties of the final perovskite film. A high concentration of MAI solution results in augmented iodine ions and reduced hole density in the CH₃NH₃PbI₃ layer. As a result, carrier density and charge transportability decrease, with low device efficiency [86]. Higher concentration of MAI contributes to more nuclei and smaller grains compared with lower concentrations of MAI [87]. The presence of impurities in the MAI solution and the polarity of the solvent also affect the morphology of the perovskite layer [86]. Post-treatments likewise thermal, solvent, and annealing treatments, also indicate significant effects on the morphology of the fabricated perovskite layer [88,89]. Fig. 10 explained the SEM images of perovskite film as a function of MAI different molarity. The SEM micrograph in Fig. 10(a) shows that the growth of the nucleation of perovskite crystal highly depends on the MAI concentration. The average grain size of the perovskites decreases with the increase in MAI concentration. A low concentration of MAI induces a low nucleation density, thereby increasing the average grain size. The surface coverage increases with the MAI concentration. In the case of 5 mg/ml MAI, untreated PbI₂ forms densely packed crystals with nanoscale dimensions (Fig. 10(b)). However, when dipped into MAI, perovskite grains form, and their number and size increase as the reaction proceeds. The grains stop growing after 1.5 min of reaction. In the top view, it is clear that there is no residual PbI₂ appear in perovskites film. The perovskite grains are sufficiently dense to prevent the penetration of MAI molecules. Thus, the chemical reaction remarkably slows down after the saturation time. In Fig. 10(c),

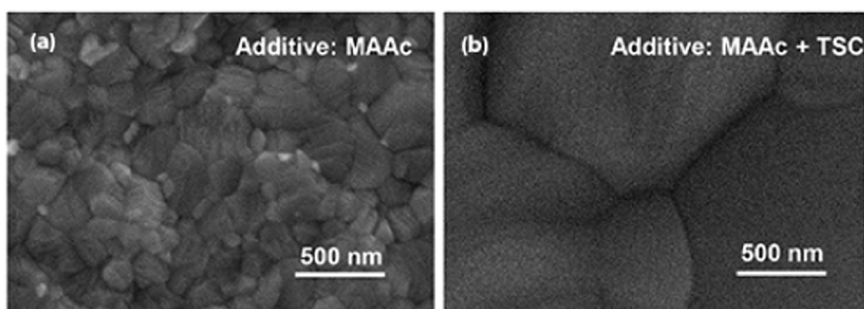


Fig. 8. SEM micrograph (Top view) of perovskite films fabricated with (a) MAAc (b) MAAc + TSC in precursor (Reprint permission from Ref. [81]).

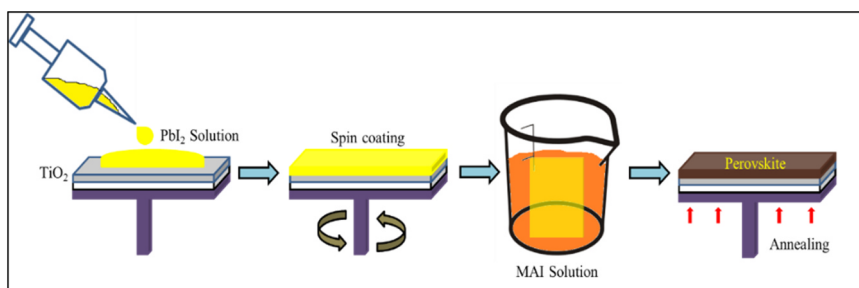


Fig. 9. Schematic illustration of fabrication method of perovskite layer by sequential deposition method.

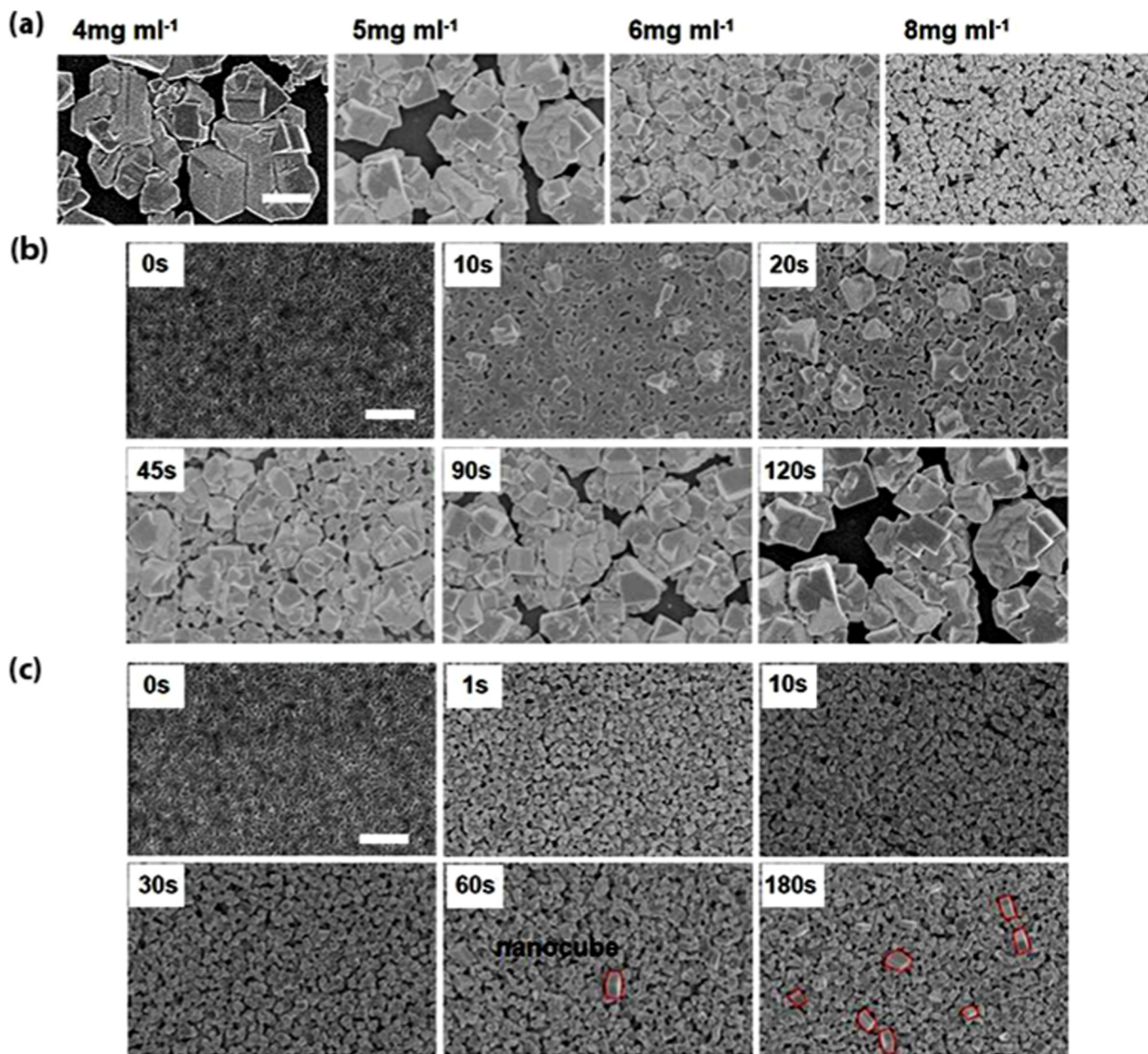


Fig. 10. SEM micrograph of $\text{CH}_3\text{NH}_3\text{PbI}_3$ from reaction with (a) different concentrations (4, 5, 6, and 8 mg/ml) of MAI (b) reaction with MAI for 0 s, 10 s, 20 s, 45 s, 90 s, and 120 s with 5 mg/ml MAI in IPA. (c) Reaction with MAI for 0 s, 1 s, 10 s, 30 s, 60 s, and 180 s with 10 mg/ml MAI. All scale bars are 1 μm (Reprint permission from Ref. [90]).

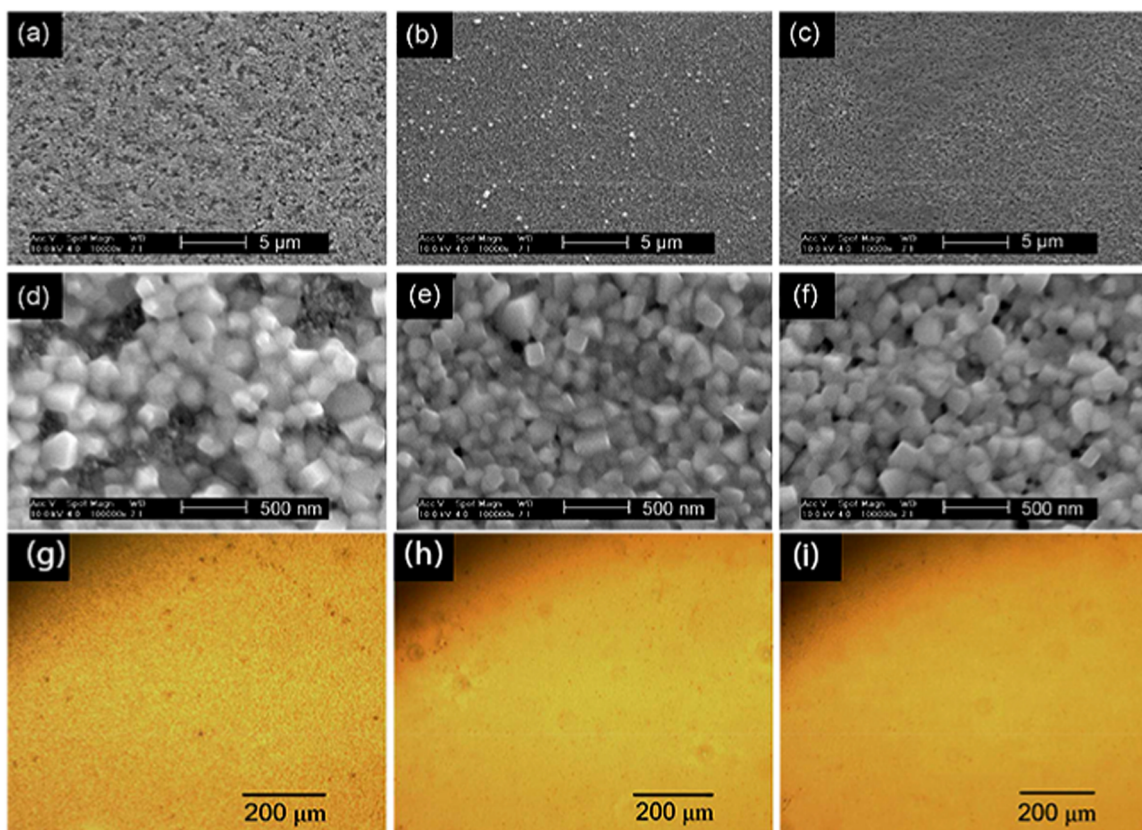


Fig. 11. Top view SEM micrograph of perovskite on mp-TiO₂ films. The PbI₂ was spin coated one (a, d), two (b, e) and three (c, f) times. Optical microscopic view of the PbI₂ films spin-coated (g) one time (h) two times, and (i) three times (Reprint permission from Ref. [92]).

when 10 mg per ml MAI is used, a lot of small CH₃NH₃PbI₃ grains initially form homogeneously. This morphology is sustained for a time; however, eventually, large single-crystal perovskite nanoplates, nanorods, and nanocubes begin to form, which indicate that single CH₃NH₃PbI₃ crystals may form by dissolution and recrystallization [90].

The PCE of PSCs can be stimulated by reducing the spinning rate and increasing the concentration of PbI₂ molecule. Fig. 11(a) and (d) indicate that uniform and pinhole-free perovskite layer on TiO₂ substrate cannot be obtained by spin coating the PbI₂ only once. The optical microscopic view reveals that the partial coverage on the TiO₂ film with perovskite crystals is mainly accredited to the relatively uneven surface of the PbI₂ films, as shown in Fig. 11(g), because the morphology of the perovskite absorber layer is mostly determined by the PbI₂ film [91]. The morphology of the PbI₂ film on TiO₂ is enhanced, and a whole coverage of perovskite on the TiO₂ film with interrelated crystals can be obtained, as shown in Fig. 11(h) by spin coating the PbI₂ solution for a second time. However, the effect of repeated spin coating of PbI₂ to improve the surface morphology remains vague, and obvious differences in the crystallisation have yet to be reported. Possible reasons that contribute to such a phenomenon could be the crystallisation-dissolution-recrystallization route and an improvement in the surface moistening, which allows the highly concentrated PbI₂ solution to cover the mp-TiO₂ film homogeneously.

2.1.2.2. Two-step spin-coating method. The two-step spin-coating method has been suggested to resolve the issue caused by the dipping method. In this method, the size of MAPbI₃ is observed and remarkably changed by the MAI conc. during the 2nd step of spin coating [87]. Fig. 12 depicts a schematic of the two-step spin-coating deposition technique. In this method, a PbI₂ layer is spin-coated over the top of the substrate and then dried. After cooling at room temperature, the

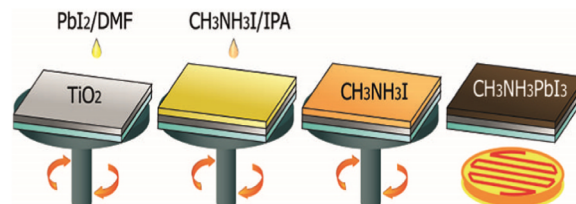


Fig. 12. Schematic diagram of obtaining perovskite layer by two-step spin-coating method.

CH₃NH₃I solution in 2-propanol is loaded again on top of the PbI₂-coated substrate by spin coating, and then dried again. This method was first proposed by Huang as a modified SDM method.

In case of single solvents, one-step spin coating is found to be poorer to two-step spin coating in terms PCE because of remarkable alterations in the morphology of MAPbI₃ [68]. The grain size of MAPbI₃ can be easily controlled by a two-step spin-coating method. For example, low concentrations produce large cuboid crystals, whereas high concentrations yield small cuboid MAPbI₃. In Fig. 13(a)–(e), the formation of MAPbI₃ cuboids is induced by the two-step spin coating procedure, and the size and shape of the cuboids are significantly biased by the MAI concentration [87]. Furthermore, the average cuboid size is approximately 720 nm for 0.038 M, and 90 nm for 0.063 M. The small cuboids are closely packed on the substrate, whereas the large cuboids have gaps between themselves and exhibit improved PCE because of enhanced internal light scattering, thereby leading to high photocurrent density (J_{sc}). However, the highest open-circuit voltage (V_{oc}) is not exhibited by the largest cuboids, but exhibits by the medium-sized cuboids. Delaying charge mobility may raise the chance of recombination, and is responsible for reducing the open circuit voltage of the largest cuboid. This result directs that the mobility for charge

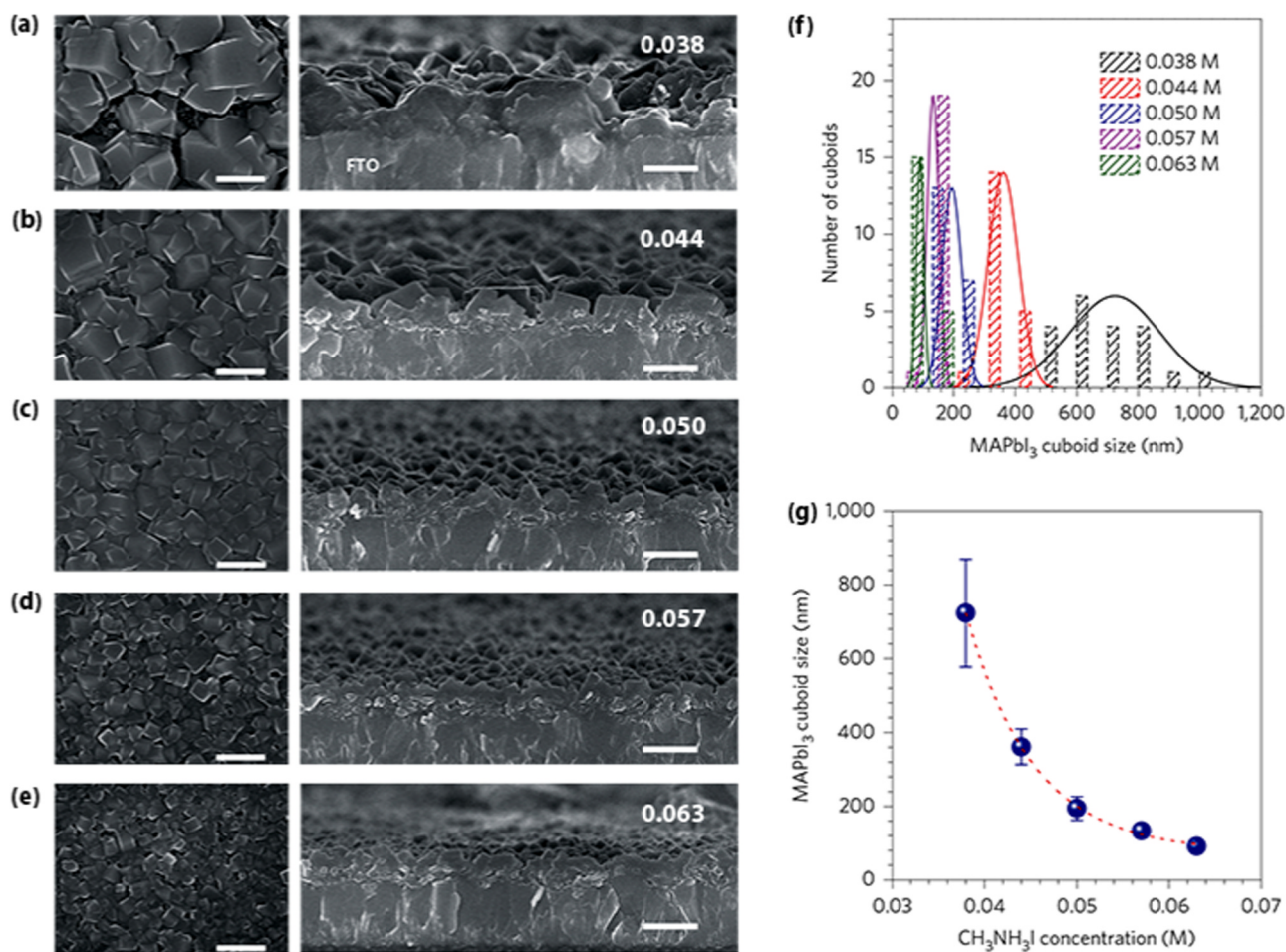


Fig. 13. Top views (left) and the cross-sectional view (right) SEM micrographs, and dependence of MAPbI₃ cuboid size on CH₃NH₃I conc. (a) 0.038 M, (b) 0.044 M, (c) 0.050 M, (d) 0.057 M, (e) 0.063 M; scale bars: 500 nm. (f) Histogram of MAPbI₃ cuboid size for CH₃NH₃I conc. from 0.038 M to 0.063 M. (Solid lines represent normal distribution curves) (g) Plot of average MAPbI₃ cuboid size versus CH₃NH₃I conc. Data (blue circles) were fit with a nonlinear curve with asymptotic exponential relation (dashed red line) (Reprint permission from Ref. [87]).

extraction acts a vital role in controlling V_{oc} . The J_{sc} increases with the size of MAPbI₃; thus, a higher J_{sc} can be expected corresponding to the larger cuboid size. However, a higher J_{sc} cannot be obtained from a few micron-sized MAPbI₃ cuboids, which are grown by further decreasing the MAI concentration. The size distribution widens with the decrease in CH₃NH₃I concentration, as shown in Fig. 13(f). The cuboid size of MAPbI₃ is plotted as a function of MAI conc. in Fig. 13(g), which illustrates an exponential decay in the cuboid size with MAI conc. An exponential function to an asymptotic plateau provides a good fit for the data, which suggests that the MAPbI₃ crystal growth strongly associated with MAI conc.

The dependence of the MAPbI₃ cuboid size on MAI conc. was studied by SEM at different loading times of 1, 5, 10, and 20 s for 0.038 M and 0.063 M MAI solution, as shown in Fig. 14. Crystal growth with waiting time is evident for the 0.038 M CH₃NH₃I solution, whereas no crystal growth occurs with waiting time for the higher conc. of 0.063 M. For 0.038 M, the growth in size is reduced possible by the low CH₃NH₃I concentration because the seed crystals are thinly distributed (Fig. 14(a)). This situation is also indicative of localised nucleation. In contrast to low-conc. case, further crystal growth is obstructed at the higher conc. because nucleation and growth are already completed at the initial stage (1 s), as shown in Fig. 14(b). The colour changed from light brown to dark black for the 0.038 M case; however, no change in colour was observed for the 0.063 M case [87].

2.2. Vapour-assisted processing

2.2.1. VASP

Snaith et al. proposed the VASP to avoid the pinhole formation issues within the perovskite films during perovskite layer deposition [85]. This process is a modification of the SDM, as shown in Fig. 15. This method is also known as two-step hybrid deposition. In this method, a PbI₂ layer is spin-coated over the top of the substrate, and MAI is then deposited through a vapour deposition technique rather than a solution-dipping process [5].

The VASP is based on the kinetic reactivity of MAI and the thermodynamic stability of perovskite during the growth process, and offers films with certain grain structure, large crystal sizes, entire surface coverage, and negligible surface roughness that are suitable for PV applications. Morphology and grain size can be controlled by this method via gas–solid crystallisation. However, this method is limited in gas–solid reactions [82]. The PCE of PSCs based on films prepared via the VASP method reaches up to 12.1%, which is thus far the highest PCE in PSC with a planar structure [87].

Fig. 16 shows the CH₃NH₃PbI₃ films deposited on the top of FTO-coated glass with a compact TiO₂ layer via VASP method. Fig. 16(a) shows corresponding XRD of the as-prepared perovskite film. Orthorhombic crystal structure of MAPbI₃ with high crystallinity is obtained due to the presence of strong peaks at 14.08°, 28.41°, 31.85°, and 43.19°

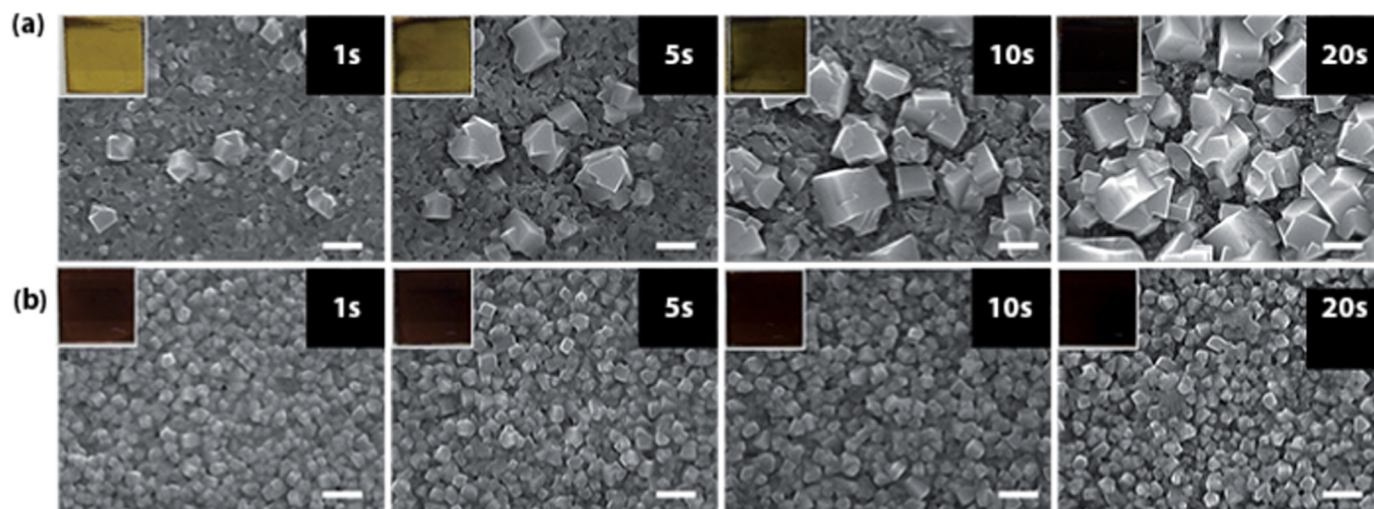


Fig. 14. SEM micrograph at different loading times (1, 5, 10, 20 s) for the (a) 0.038 M and (b) 0.063 M $\text{CH}_3\text{NH}_3\text{I}$ (Reprint permission from Ref. [87]).

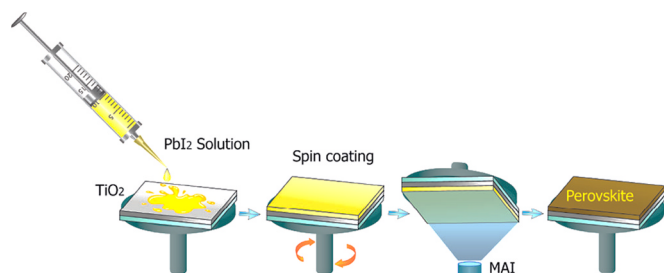


Fig. 15. Schematic illustration for obtaining perovskite layer by vapour-assisted solution process.

[88,89]. The absence of any small signature peak at 12.65° endorses the absence of unchanged PbI_2 film, and suggests a complete consumption of PbI_2 via the VASP [90]. Fig. 16(b) shows the top-view SEM image of perovskite film covering the full surface of the substrate, with remarkable grain size up to the micro scale. The surface roughness measured by AFM is shown in Fig. 16(c) and is calculated to be 23.2 nm. The film roughness is smaller compared with other solution process techniques [19]. The cross-sectional SEM micrograph of MAPbI_3 film on the $\text{FTO}/\text{c-TiO}_2$ substrate reveals definite grain structure with a 350 nm thickness (Fig. 16(d)). Uniform grain structure, microscale grain size, and full surface coverage indicate the pertinence of use in PV devices [87]. Nevertheless, the SEM image of the VASP confirms almost zero pinholes compared with solution-processed thin films. Chen et al. reported on perovskite layers formed by the VASP and SDM on top of a TiO_2 scaffold, which shows the distinctive properties of PL emission spectra. They concluded that perovskite films prepared by the SDM could not effectively extract excitons from the layer. They also proved that the perovskite film formed by the SDM contained a higher exciton lifetime when deposited on top of TiO_2 than with vapour-phase deposition. These findings indicated that the SDM caused the defect densities that accumulated on perovskite films.

2.2.2. TVD

TVD for the perovskite absorber layer was first introduced by David B. Mitzi, and was reproduced by Liu et al. for planar heterojunction $\text{MAPbI}_{3-x}\text{Cl}_x$ PSCs with a PCE of 15.4% [17]. In this method, MAPbI_3 absorber was deposited by a dual-source evaporation system in a nitrogen-filled glove box. The compact layer was initially deposited atop FTO coated glass. Vapour-deposited perovskite films were then fabricated atop the compact layer. Extremely uniform and total surface area coverage are the main advantages of the TVD method, but controlling

the vapour phase reaction is crucial. In this method, MAX and PbX_2 are simultaneously evaporated from different sources at definite molar ratios under high vacuum, as shown in Fig. 17. A film of dark reddish-brown was obtained after evaporation, and then annealed [17].

The top and cross-sectional views of the SEM micrograph of perovskite film deposited by vapour deposition are shown in Figs. 18(a) and 18(b). Fig. 18(a) illustrates that the vapour-deposited films are tremendously uniform, and cover the entire surface area of the TiO_2 compact layer with a length scale of hundreds of nanometres. The cross-sectional images of the completed PSC devices roughly reveal evidence of the crystal size (Fig. 18(b)). The vapour-deposited perovskite film is flat and uniform, with slightly larger crystal features [17].

After deposition, the colour of the perovskite film varies depending on the composition of PbX_2 and MAX. Reddish-brown perovskite film is observed for the best performing PSCs, and films are shown partially crystallised in the topological SEM image of the as-deposited film (Fig. 18(c)). Annealing perovskite films in the N_2 -filled glove box facilitates full crystallisation of the perovskite, darkens the colour, and results in the apparent growth of the crystal features visible in the SEM micrograph, as shown in Fig. 18(d) [17]. Afterwards the deposition of thermally evaporated perovskite, annealing significantly affects the outstanding crystal growth and film quality. Fig. 19(a) and (b) show the morphology of perovskite before and after annealing, respectively. Perovskite film studied after immediate deposition reveals a complex morphology, with a homogeneous and unstructured under layer with a few arbitrarily dispersed greater aggregates. After annealing, the MAPbI_3 perovskite film changes to a highly diverse morphology with homogeneously distributed perovskite polycrystals with sizes between 100 nm and 200 nm and well-defined terracing, thereby entirely covering the substrate [94]. The outcome recommends the formation of a crystalline MAPbI_3 film, which is alike to that earlier reported by Yu et al. on spin-coated perovskite films. XRD patterns in the insets of Fig. 19(a) and (b) disclose the cubic phase of perovskite and similar peak intensity enhancement after annealing, indicating that perovskite evolution is not hindered by the underlying film [95].

2.2.3. CVD

CVD has been considered a mature industrial technology for the fabrication of perovskite film, and has been widely used in commercial deposition [96,97]. Generally, CVD covers tubular CVD, metal-organic CVD, plasma-enhanced CVD and photo-initiated CVD. [96,98–102]. The tubular CVD method has been successfully applied for the deposition of PSCs and has revealed outstanding results [103,104]. The process parameters of tubular CVD, such as reaction temperature, growth ambient environment, and vapour pressure can be effectively controlled

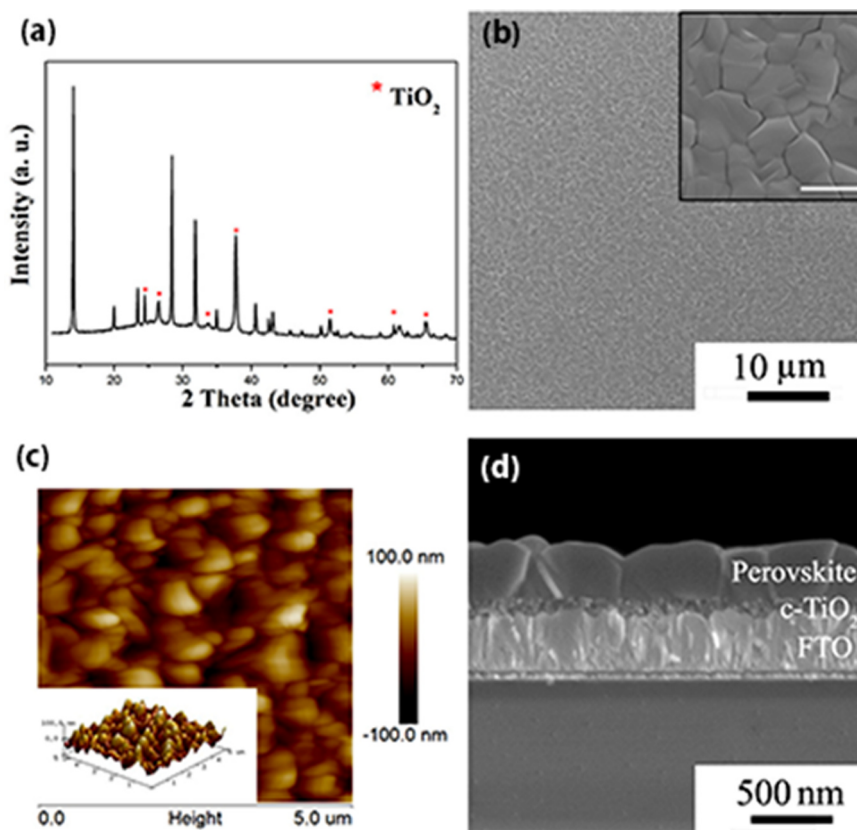


Fig. 16. (a) XRD pattern; (b) Top-view SEM micrograph (inset image with higher resolution) (c) Tapping-mode AFM height images (inset is the corresponding 3D topographic image); (d) Cross-sectional SEM micrograph of MAPbI₃ film via VASP on the FTO/c-TiO₂ substrate (Reprint permission from Ref. [93]).

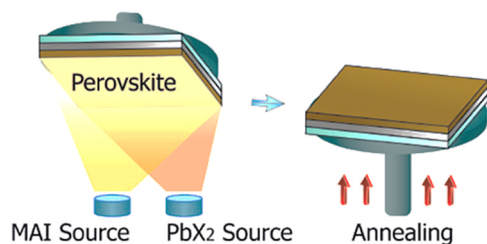


Fig. 17. Schematic illustration of the thermal vapour deposition process.

in a small quartz chamber. Notably, the slow gas-phase reaction nature can reduce the over-rapid inserting reaction rate in perovskites, which accordingly produces smooth and uniform perovskite films [103]. Hybrid CVD (HCVD) and low-pressure CVD (LPCVD) are widely used CVD methods for perovskite deposition. However, rest of the CVD methods are not used in practice because they require complex fabrication tools.

2.2.3.1. HCVD. In 2014, Qi et al. first introduced HCVD technology for the effective deposition of a perovskite layer [104]. Vacuum thermal evaporation and gas-phase deposition were chronologically used to fabricate perovskite films. In this method, PbX₂ was initially evaporated in a high-vacuum environment to obtain uniform films, and MAI was then heated to 185 °C and transported into the reaction site by N₂ gas. Finally, a post-annealing process was conducted on the as-prepared films in an air or glove box. A schematic of the HCVD method is shown in Fig. 20. In this method, growth temperature is the key factor for fabricating high-quality perovskite films. A higher temperature did not ensure perovskite film formation, whereas films formed at a lower temperature were unstable in air.

On the basis of the relation between the gas diffusion constant, growth temperature, and gas pressure, the gas diffusion rate should be

effectively tuned by an optimal combination of temperature and pressure [105]. Given that the growth temperature is limited to approximately 170 °C, the diffusion rate in HCVD can be varied over a wide range by controlling its gas pressure. Thus, high-quality perovskite films with smooth, fully covered surfaces are achieved by using the HCVD method [106]. Leyden et al. showed the influence of the thickness of the pre-deposited lead halide layer and successive MAPbI₃ on the average PCE of PSCs. Fig. 21(a) and (b) indicate that a peak with the best efficiency is evident at a lead halide layer thickness of ≈ 100 nm, which corresponds to ≈ 300 nm thick MAPbI₃ films [104]. The surface morphology after air annealing was different from surfaces annealed in a N₂ environment. Perovskite films annealed in air resulted in higher PSC performance compared with films obtained from N₂ annealing, providing a maximum efficiency of 11.8% and an average PCE of 10.8%; whereas N₂-annealed perovskite films resulted in an average efficiency of 6.1% and a maximum of 8.8%. In addition, these cells retained nearly the same PV performance after around 46 days of storage in dry N₂ gas, thereby exhibiting excellent stability.

Fig. 21(c) shows a photograph of a completed and functioning device by the HCVD method forecast, where the film is partially transparent and homogeneous. Fig. 21(d) presents the absorbance spectrum of a completed device, where the absorption edge is measured at 781 nm [42], thereby making the approach suitable for applications that include PV windows and multi-junction solar cells [107].

2.2.3.2. Ambient atmosphere vapour-assisted deposition. In 2016, Zheng et al. reported another significant two-step HCVD method, and achieved the highest efficiency among vapour-based routes. High-quality perovskite films in open air have been fabricated by this method, which was considered a significant progress in the CVD fabrication of PSCs. In this method, the heating source was altered using hot airflow through the outer tube in lieu of normally used

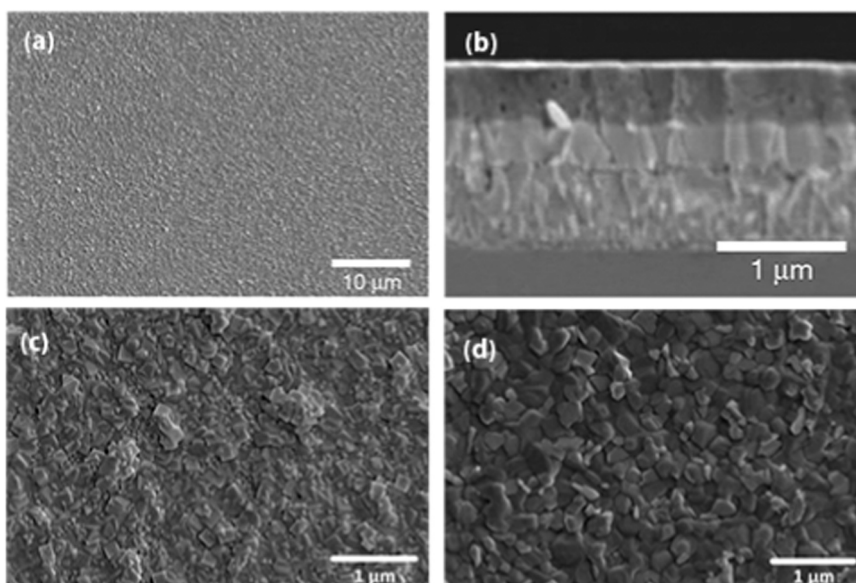


Fig. 18. SEM micrograph of (a) top view of perovskite film and (b) cross-sectional view of complete PSCs by thermal vapour-deposition method. Top-view SEM micrograph showing (c) as deposited (d) post-annealed vapour deposited perovskite films (Reprint permission from Ref. [17]).

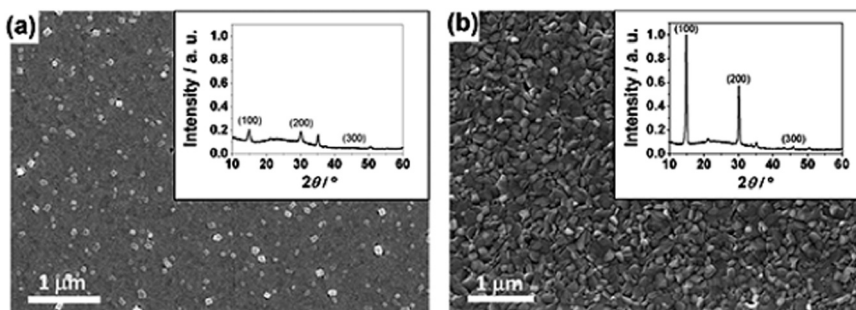


Fig. 19. (a) SEM micrograph of the MAPbI₃ film by thermal evaporation method on top of PEDOT:PSS (after deposition), and (b). XRD patterns (after thermal annealing) are shown in inset (Reprint permission from Ref. [94]).

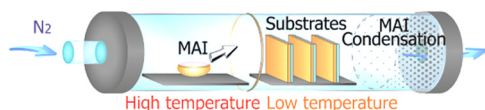


Fig. 20. Schematic illustration of HCVD for the deposition of MAPbI₃ layer.

electrothermal method. The airflow was produced from a heat gun that controlled the flow rate and temperature. MAI vapour was transported onto the PbI₂ substrate via a carrier gas, which was also injected as hot air through the provided hole at the head of the inner glass tube. The humidity of the reaction chamber was strictly controlled, and the relative humidity (RH) was maintained at one-fourth of the ambient RH value. A schematic of the ambient atmosphere vapour-assisted deposition technique is shown in Fig. 22.

Photographs of perovskite film fabricated by the ambient atmosphere vapour-assisted deposition method on an FTO/cTiO₂ substrate, top-view and cross-sectional micrographs of as-grown perovskite film are shown in Fig. 23(a)–(c). A uniform perovskite film thickness with dense surface morphology and large crystal domains can be observed from the surface and cross-sectional SEM images. The fabrication method is completely performed in an ambient atmosphere, and exhibits high environmental tolerance. This approach is an effective technology for fabricating PSCs for commercialisation [108].

2.2.3.3. LPCVD. The LPCVD method was first introduced in the fabrication of PSCs by Luo et al. in 2015 [103]. LPCVD technology can meritoriously minimise the over-rapid intercalating reaction rate and easily overcome this blocking issue during the solution process. Perovskite films obtained by the LPCVD method displays good crystallisation, strong absorption, long carrier diffusion length, and exceptional humid resistant features even under laser illumination and high-temperature conditions [97,100]. A schematic of the LPCVD method is shown in Fig. 24.

In the LPCVD deposition technique, PbI₂ precursor films are first prepared by spin coating. After vacuum pumping for pressure reduction, MAI powder and PbI₂ film are placed in heating zones A and B, respectively, and are heated separately at different temperatures. The MAI vapour reacts with the PbI₂ precursor film via a gas–solid reaction process. Low cost, low energy consumption and high reaction yield are the main advantages of the LPCVD method. MAPbI₃ films with good crystallisation, long carrier diffusion length, strong absorption, and high stability have been achieved by the LPCVD technique [106]. Morphology and the composition of the perovskite absorber are the main indicators for attaining highly efficient PSCs. Thus, smooth, nonporous and compact MAPbI₃ films must be attained to prevent the shunt current that generally arises from direct contact with the corresponding charge carrier layers. The solution-based process consistently

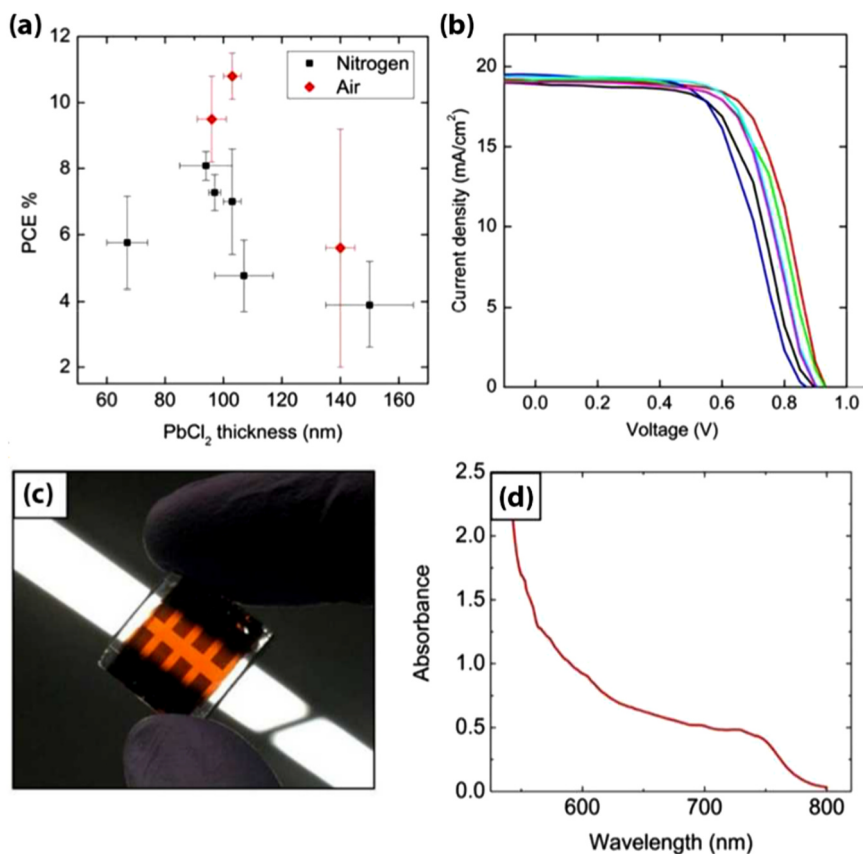


Fig. 21. a) PCE as a function of film thickness, N_2 (black dots) and air annealed (red dots) b) I-V Curve (c) HCVD SCs with front illumination from a fluorescent light bulb (d) UV-vis spectrum of a complete cell (Reprint permission from Ref. [104]).



Fig. 22. Schematic diagram of the ambient atmosphere vapour-assisted deposition method.

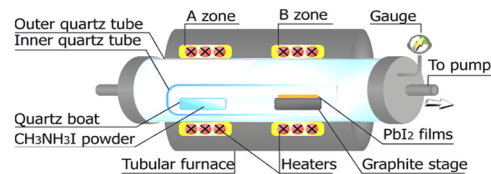


Fig. 24. Schematic diagram of LPCVD instrument.

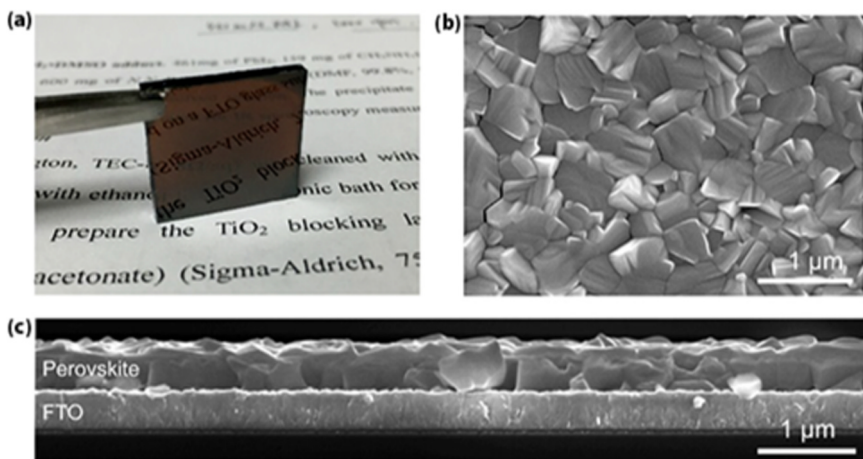


Fig. 23. (a) Photographs of the as-deposited $MAPbI_3$ film on FTO/c- TiO_2 substrate. SEM micrographs of (b) the top-view, and (c) cross-sectional image of the as-deposited $MAPbI_3$ film (Reprint permission from Ref. [108]).

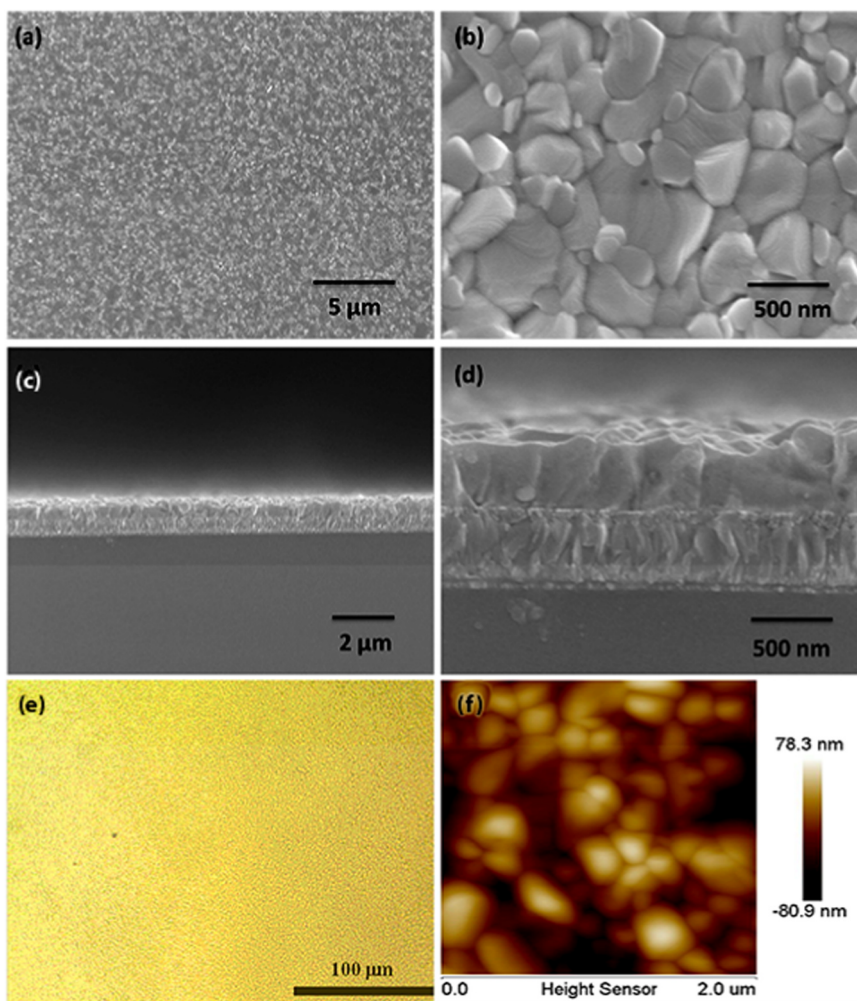


Fig. 25. Low and high magnification top surface (a-b) and cross-sectional (c-d) SEM micrographs of $\text{CH}_3\text{NH}_3\text{PbI}_3$ absorbers. (e) Metallurgical micrograph, and (f) 2-D AFM height image of $\text{CH}_3\text{NH}_3\text{PbI}_3$ absorbers (Reprint permission from Ref. [103]).

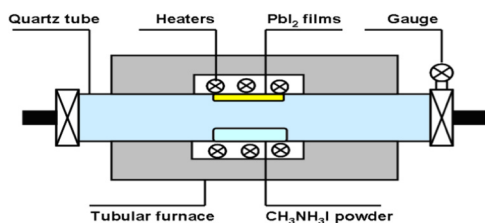


Fig. 26. Schematic diagram of in situ chemical vapour deposition (ITCVD) equipment.

produces bare pinholes and large grains [19,70]; nevertheless, the LPCVD technique exhibits better morphology, which has been verified by AFM, SEM, and metallurgical microscopy, as shown in Fig. 25.

The SEM investigation in Fig. 25(a)–(d) reveals that a homogeneous, uniform, and well-defined perovskite layer can be obtained by the LPCVD technique. The metallurgical micrograph in Fig. 25(e) indicates that films deposited by the LPCVD method are extremely dense and compact, and have super uniformity, which indicate a high level of crystallisation. The 2-D AFM height image in Fig. 25(f) shows that the calculated roughness of the homogenous films is only 19.6 nm. The bearing depth over a $2 \times 2 \mu\text{m}$ 3-D AFM graph is also only 78 nm.

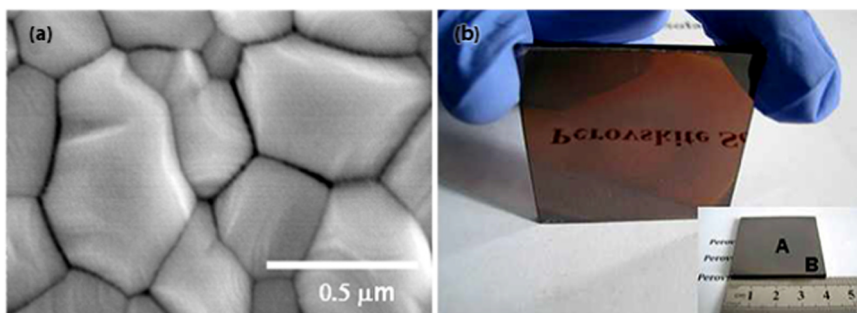


Fig. 27. a) SEM of perovskite films, and b) photographs of large demonstrated sample via ITCVD (Reprint permission from Ref. [109]).

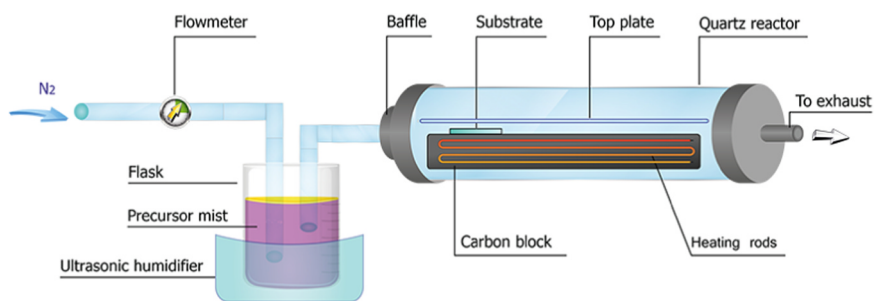


Fig. 28. Schematic diagram of AACVD instrument.

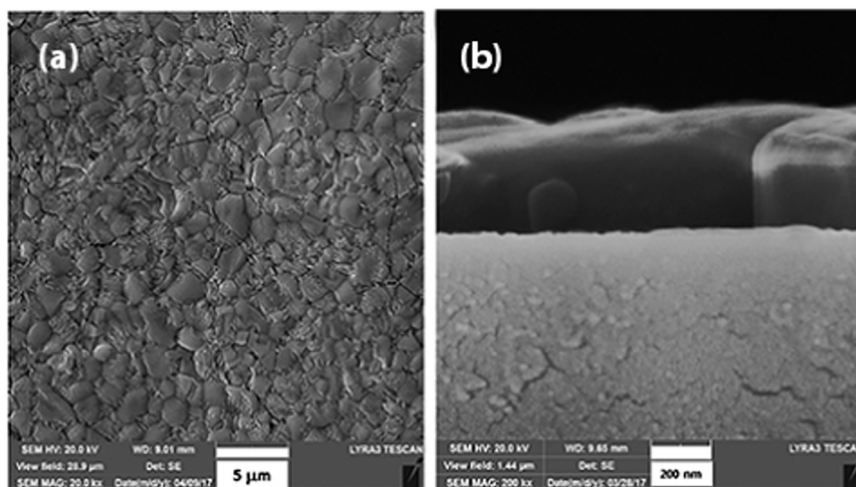


Fig. 29. SEM micrograph of (a) top, and (b) cross-sectional view of complete PSCs using AACVD (Reprint permission from Ref. [111]).

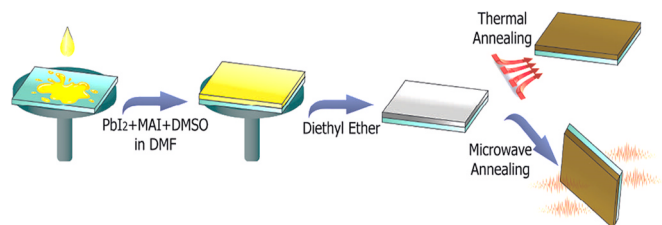


Fig. 30. Schematic diagram of microwave irradiation process (MIP) equipment.

2.2.3.4. In situ tubular chemical vapour deposition (ITCVD). Solution-based technology and the thermal evaporation route remain challenging for producing low-cost, large-scale, and highly uniform perovskite absorber layers. Luo et al. proposed the ITCVD technique to overcome the aforementioned limitations [109]. The main advantages of ITCVD are its cost-effectiveness and minimal equipment requirements, such as glove box or vacuum instruments [17,110]. The approach can potentially be applied to large surface area deposition. In comparison with HCVD and LPCVD, only time and temperature must be controlled, which indicates that ITCVD is easier to control than other thermal techniques. A schematic of ITCVD equipment is shown in Fig. 26.

In the ITCVD technique, a PbI_2 solution is initially spin-coated on top of the compact TiO_2 film. The lead halide-coated FTO/ITO substrate is then directly positioned at the top of the MAI vapour, and heated at a specific temperature for a specified period. Thereafter, the reacted film is removed and washed with 2-propanol, and annealed at 145°C for 30 min in ambient environment. The SEM micrograph in Fig. 27(a) indicates that the ITCVD technique produces dense and precise perovskite film with grain sizes at the submicron level. An interesting feature of the ITCVD technique is that it provides large-size samples,

which indicate its ability to scale in future mass production (Fig. 27(b)).

2.2.3.5. Aerosol-assisted chemical vapour deposition (AACVD). To obtain thick and uniform perovskite thin film, a modified three-step AACVD method was proposed by Afzal et al. [111]. However, the AACVD method was originally introduced by Chen in 2016 [112]. A solution-based AACVD method using aerosol droplets to transport precursors provides an alternative for depositing perovskite films at ambient pressure. Several research groups have validated a one-step AACVD method to deposit perovskite thin films [113,114], but the deposited films were likely to be of low density and composed of powdery agglomerates due to early gas-phase nucleation between lead halide and MAI at the deposition temperatures. Compared with other deposition methods, AACVD is a low-cost and scalable technique. Although dense and uniform perovskite film can be grown by the AACVD method, the growth process is very challenging. A schematic of the AACVD method is shown in Fig. 28.

In the AACVD deposition technique, a cold-walled horizontal-bed AACVD reactor was used to deposit perovskite film. The system was continuously purged with N_2 before conducting the experiment to reduce moisture and contaminants. In the first step, PbI_2 films are prepared by using an aerosol of PbI_2 in DMF for 1 h. In the second step, DMF is evaporated at 70°C for 5 min. After evaporating the DMF, an MAI solution is introduced into the system via aerosol at 220°C (third stage) for 1 h. The N_2 gas is passed through the reactor during the course of the experiment. After deposition, the films are immediately removed from the reactor and transferred to an N_2 glove box. Afzal et al. showed the formation of stable tetragonal high-quality perovskite structures with minor impurity and strong absorption and emission characteristics at room temperature using the three-step AACVD method. The SEM micrographs are shown in Fig. 29(a) display a dense and pinhole-free perovskite film grown by the AACVD method. The

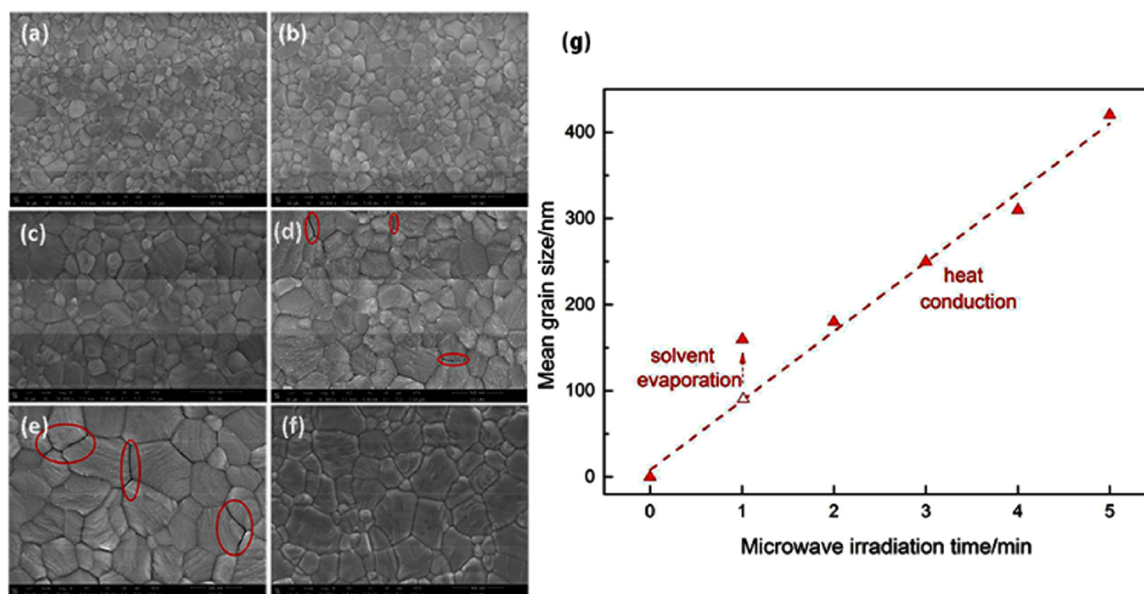


Fig. 31. Top-view of SEM micrograph of MAPbI₃ films treated by 160W microwave irradiation for (a) 1, (b) 2, (c) 3, (d) 4, (e) 5min, and (f) annealing at 100°C for 10min. (g) Time dependence of mean grain size of MAPbI₃ film under 160 W microwave irradiation (Reprint permission from Ref. [115]).

cross-sectional view in Fig. 29(b) confirms a uniform film with an average thickness of 400 nm.

2.2.4. MIP

In 2016, Cao et al. first introduced the MIP for the deposition of perovskite films [115]. The MIP is a non-contact, rapid, and selective heating method that has been widely applied in OPVs [116,117]. The MIP is a one-step process in which microwave irradiation is used to treat the perovskite film for several minutes at a fixed output power.

In this method, the MAPbI₃ precursor is prepared, followed by a method reported by Ahn et al. in which PbI₂, CH₃NH₃I, and DMSO with a molar ratio of 1:1:1 are mixed in dry DMF solution at room temperature and stirred for 60 min. Then, the MAPbI₃ precursor is spin-coated on the mp-TiO₂, and 0.5 ml of (C₂H₅)₂O is dripped on the spinning substrate, which is then annealed at different temperature. At first, the samples are positioned on a Teflon shelf and then in a microwave oven (160 W) for several minutes [118]. A schematic of the MIP is shown in Fig. 30. In the MIP, the solvent is evaporated directly and the perovskite film forms quickly. In a compare with other annealing processes, the MIP assists fast and controllable crystallisation of MAPbI₃ films with minimal energy input and time consumption [115].

The effect of microwave irradiation duration on the morphology of MAPbI₃ film is illustrated in Fig. 31(a)–(f); the figures indicate that perovskite is uniformly distributed over the substrate. Fig. 31(g) shows that the trend of the corresponding grain size of the MAPbI₃ films linearly increases with the duration of microwave irradiation treatment. Thus, the grain size of the MAPbI₃ film can be regulated by altering the time allowed for microwave irradiation treatment. Given that the growth rate of MAPbI₃ grains is sensitive to the annealing rate and temperature, the crystallisation of MAPbI₃ film can be controlled by accurately varying the power and time of microwave irradiation. At long irradiation periods, some grain boundaries shrink and show cracks between the grains, as shown in Fig. 31(d) and (e) [115].

3. Future outlook

Among the existing renewable energy technologies available today, PV technologies are the most promising and fastest-growing technologies that may offer a solution to the upcoming energy crisis. Of all PV technologies, lead halide PSCs have drawn considerable attention and interest due to their rapid growth in power conversion efficiency.

However, the most challenging aspect of PSCs is to grow a hydrophobic perovskite layer that can produce a stable and high-performance perovskite device. This can be achieved through the surface modification of the perovskite layer via additives, ionic liquids, and hydrophobic moiety. Toxic lead is another critical drawback for PSCs. New inorganic materials must be found to replace toxic lead. To minimise the cost of PSCs, researchers should focus on depositing the perovskite under ambient conditions. Narrow bandgap perovskite materials and plasmonic PVs are expected to usher in a new era of light harvesting technology. Future research should include studies on the effects of defect type, defect density, and associated PV effect mechanisms. Development of stable and efficient lead halide PSCs demands advance studies to develop new materials and device structures to mitigate the future power crisis.

4. Conclusion

In this review, we provide an outline of the deposition techniques that control the structure and morphology of the perovskite layer and ultimately regulate the PCE and stability of PSCs. The film quality of perovskite plays a significant role in determining the overall performance of solar cells, such that perovskite films with high phase purity, low structural defects, suitable morphology, high crystallinity, and appropriate deposition technique with respect to the processing condition and composition of the perovskite precursor are required. Annealing temperature, film thickness, and substrate materials are the key parameters that affect the film quality in the OSD method. Pinhole formation and slow crystallisation are challenges in the OSD method; however, the dripping of anti-solvent controls the kinetics of crystal growth with a large grain size. SDM decreases the surface roughness and reduces the pinholes of the perovskite absorber layer. The disparity of grain size and surface smoothness is one shortcoming of the SDM, because surface smoothness decreases with the increase in grain size. Another drawback is the incomplete conversion of perovskite. The crystal size of MAPbI₃ can be easily controlled by a two-step spin-coating method. A low concentration of MAI produces a large cuboid crystal, whereas a high concentration yields small cuboid MAPbI₃. The VASP is based on the kinetic reactivity of MAI and thermal stability of MAPbI₃ during the growth process, and offers films with certain grain structure along with grain sizes, entire surface coverage, and minor surface roughness that are suitable for PV applications. Morphology and

grain size can be controlled by this method via gas–solid crystallisation. However, this method is limited in gas–solid reactions. Extremely uniform surface coverage, a lack of pinholes, and large grain size are advantages of TVD; however, TVD requires a long time for deposition, and controlling the temperature is difficult. CVD is considered a mature industrial technology and is widely used in commercial deposition. Reaction temperature, growth ambient condition, and vapour pressure can be effectively controlled using the CVD method. The MIP is a non-contact, rapid, and selective heating method. In comparison with other thermal annealing processes, the MIP assists in the rapid and controllable crystallisation of perovskite films with minimal energy loss and time consumption. Many studies are ongoing among PV research communities for the commercialisation of PSCs. Unprecedented growth efficiency within a short time is expected, although objections remain concerning stability, use of toxic lead, and flexible substrate issues. Given that the PSC indicates excellent optical and electrical properties, high PCE, and cheap and facile film quality, we anticipate that new solar technology based on perovskite is promised for the future PV market.

Acknowledgement

This work is supported from the Fundamental Research Grant Scheme (FRGS) with code FRGS/1/2017/TK07/UKM/02/9 of the Ministry of Higher Education, Malaysia (MOHE). This study is also supported by Bangabandhu Science and Technology Fellowship Trust under the Ministry of Science and Technology, Peoples Republic of Bangladesh.

References

- Chapin DM, Fuller C, Pearson G. A new silicon p-n junction photocell for converting solar radiation into electrical power. *J Appl Phys* 1954;25(5):676–7.
- Green MA. Silicon solar cells: evolution, high-efficiency design and efficiency enhancements. *Semicond Sci Technol* 1993;8(1):1.
- Green MA, Emery K, Hishikawa Y, Warta W, Dunlop ED. Solar cell efficiency tables (Version 45). *Progress Photovolt: Res Appl* 2015;23(1):1–9.
- Gangopadhyay U, Jana S, Das S, editors. State of art of solar photovoltaic technology. In: Proceedings of the conference papers in science, Hindawi Publishing Corporation; 2013.
- Song Z, Wathage SC, Phillips AB, Heben MJ. Pathways toward high-performance perovskite solar cells: review of recent advances in organo-metal halide perovskites for photovoltaic applications. *J Photonics Energy* 2016;6(2):022001.
- Yang J, Siempelkamp BD, Liu D, Kelly TL. Investigation of CH₃NH₃PbI₃ degradation rates and mechanisms in controlled humidity environments using in situ techniques. *ACS Nano* 2015;9(2):1955–63.
- You J, Yang Y, Hong Z, Song T-B, Meng L, Liu Y, et al. Moisture assisted perovskite film growth for high performance solar cells. *Appl Phys Lett* 2014;105(18):183902.
- Dan-Fei Z, Ling-Ling Z, Ying-Zhuang M, Shu-Feng W, Zu-Qiang B, Chun-Hui H, et al. Factors influencing the stability of perovskite solar cells. *Acta Phys Sinica* 2015;64:3.
- Brown GF, Wu J. Third generation photovoltaics. *Laser Photonics Rev* 2009;3(4):394–405.
- Chowdhury TH, Islam A, Mahmud Hasan A, Terdi M, Arunakumari M, Prakash Singh S, et al. Prospects of graphene as a potential carrier-transport material in third-generation solar cells. *Chem Rec* 2016;16(2):614–32.
- Conibeer G. Third-generation photovoltaics. *Mater Today* 2007;10(11):42–50.
- Szweda R. Third generation solar cells III-Vs. *Reviews* 2003;16(6):53–5.
- Yin W, Pan L, Yang T, Liang Y. Recent advances in interface engineering for planar heterojunction perovskite solar cells. *Molecules* 2016;21(7):837.
- Gao P, Grätzel M, Nazeeruddin MK. Organohalide lead perovskites for photovoltaic applications. *Energy Environ Sci* 2014;7(8):2448–63.
- Shi S, Li Y, Li X, Wang H. Advancements in all-solid-state hybrid solar cells based on organometal halide perovskites. *Mater Horiz* 2015;2(4):378–405.
- Boix PP, Nonomura K, Mathews N, Mhaisalkar SG. Current progress and future perspectives for organic/inorganic perovskite solar cells. *Mater Today* 2014;17(1):16–23.
- Liu M, Johnston MB, Snaith HJ. Efficient planar heterojunction perovskite solar cells by vapour deposition. *Nature* 2013;501(7467):395–8.
- Jeon NJ, Noh JH, Yang WS, Kim YC, Ryu S, Seo J, et al. Compositional engineering of perovskite materials for high-performance solar cells. *Nature* 2015;517(7535):476–80.
- Burschka J, Pellet N, Moon S-J, Humphry-Baker R, Gao P, Nazeeruddin MK, et al. Sequential deposition as a route to high-performance perovskite-sensitized solar cells. *Nature* 2013;499(7458):316–9.
- Yang WS, Park B-W, Jung EH, Jeon NJ, Kim YC, Lee DU, et al. Iodide management in formamidinium-lead-halide-based perovskite layers for efficient solar cells. *Science* 2017;356(6345):1376–9.
- Kojima A, Teshima K, Shirai Y, Miyasaka T. Organometal halide perovskites as visible-light sensitizers for photovoltaic cells. *J Am Chem Soc* 2009;131(17):6050–1.
- Xu T, Chen L, Guo Z, Ma T. Strategic improvement of the long-term stability of perovskite materials and perovskite solar cells. *Phys Chem Chem Phys* 2016;18(39):27026–50.
- Salhi B, Wudil Y, Hossain M, Al-Ahmed A, Al-Sulaiman F. Review of recent developments and persistent challenges in stability of perovskite solar cells. *Renew Sustain Energy Rev* 2018;90:210–22.
- Ansari MIH, Qurashi A, Nazeeruddin MK. Frontiers, opportunities, and challenges in perovskite solar cells: a critical review. *J Photochem Photobiol C: Photochem Rev* 2018;35:1–24.
- Ma Y, Wang S, Zheng L, Lu Z, Zhang D, Bian Z, et al. Recent research developments of perovskite solar cells. *Chin J Chem* 2014;32(10):957–63.
- Ozin G. The single crystal Raman spectrum of orthorhombic PbCl₂. *Can J Chem* 1970;48(18):2931–3.
- Weber D. CH₃NH₃PbX₃, ein Pb (II)-system mit kubischer perovskitstruktur/CH₃NH₃PbX₃, a Pb (II)-system with cubic perovskite structure. *Z für Naturforsch B* 1978;33(12):1443–5.
- Kulkarni SA, Baikie T, Boix PP, Yantara N, Mathews N, Mhaisalkar S. Band-gap tuning of lead halide perovskites using a sequential deposition process. *J Mater Chem A* 2014;2(24):9221–5.
- Borriello I, Cantele G, Ninno D. Ab initio investigation of hybrid organic-inorganic perovskites based on tin halides. *Phys Rev B* 2008;77(23):235214.
- Noh JH, Im SH, Heo JH, Mandal TN, Seok SI. Chemical management for colorful, efficient, and stable inorganic–organic hybrid nanostructured solar cells. *Nano Lett* 2013;13(4):1764–9.
- Jeon NJ, Noh JH, Kim YC, Yang WS, Ryu S, Seok SI. Solvent engineering for high-performance inorganic–organic hybrid perovskite solar cells. *Nat Mater* 2014;13(9):897–903.
- Ogomi Y, Morita A, Tsukamoto S, Saitho T, Fujikawa N, Shen Q, et al. CH₃NH₃Sn x Pb (1-x) I₃ Perovskite solar cells covering up to 1060 nm. *J Phys Chem Lett* 2014;5(6):1004–11.
- Colella S, Mosconi E, Fedeli P, Listorti A, Gazza F, Orlandi F, et al. MAPbI₃-xCl_x mixed halide perovskite for hybrid solar cells: the role of chloride as dopant on the transport and structural properties. *Chem Mater* 2013;25(22):4613–8.
- Tanaka K, Takahashi T, Ban T, Kondo T, Uchida K, Miura N. Comparative study on the excitons in lead-halide-based perovskite-type crystals CH₃ NH₃ PbBr₃ CH₃ NH₃ PbI₃. *Solid State Commun* 2003;127(9):619–23.
- Ishihara T. Optical properties of PbI₂-based perovskite structures. *J Lumin* 1994;60:269–74.
- Hirasawa M, Ishihara T, Goto T, Uchida K, Miura N. Magnetoabsorption of the lowest exciton in perovskite-type compound (CH₃NH₃) PbI₃. *Phys B: Condens Matter* 1994;201:427–30.
- Tao SX, Cao X, Bobbert PA. Accurate and efficient band gap predictions of metal halide perovskites using the DFT-1/2 method: GW accuracy with DFT expense. *Sci Rep* 2017;7(1):14386.
- Dong Q, Fang Y, Shao Y, Mulligan P, Qiu J, Cao L, et al. Electron-hole diffusion lengths > 175 μm in solution-grown CH₃NH₃PbI₃ single crystals. *Science* 2015;347(6225):967–70.
- Shi D, Adinolfi V, Comin R, Yuan M, Alarousu E, Buin A, et al. Low trap-state density and long carrier diffusion in organolead trihalide perovskite single crystals. *Science* 2015;347(6221):519–22.
- Stranks SD, Eperon GE, Grancini G, Menelaou C, Alcocer MJ, Leijtens T, et al. Electron-hole diffusion lengths exceeding 1 μm in an organometal trihalide perovskite absorber. *Science* 2013;342(6156):341–4.
- Im J-H, Lee C-R, Lee J-W, Park S-W, Park N-G. 6.5% efficient perovskite quantum-dot-sensitized solar cell. *Nanoscale* 2011;3(10):4088–93.
- Kim H-S, Lee C-R, Im J-H, Lee K-B, Moehl T, Marchioro A, et al. Lead iodide perovskite sensitized all-solid-state submicron thin film mesoscopic solar cell with efficiency exceeding 9%. *Sci Rep* 2012:2.
- Lee MM, Teuscher J, Miyasaka T, Murakami TN, Snaith HJ. Efficient hybrid solar cells based on meso-superstructured organometal halide perovskites. *Science* 2012;338(6107):643–7.
- Robertson J, Falabretti B. Band offsets of high K gate oxides on III–V semiconductors. *J Appl Phys* 2006;100(1):014111.
- Park N-G, Miyasaka T, Grätzel M. Organic-Inorganic Halide Perovskite Photovoltaics. Springer; 2016.
- Etgar L, Gao P, Xue Z, Peng Q, Chandiran AK, Liu B, et al. Mesoscopic CH₃ NH₃ PbI₃/TiO₂ heterojunction solar cells. *J Am Chem Soc* 2012.
- Chen Q, Zhou H, Hong Z, Luo S, Duan H-S, Wang H-H, et al. Planar heterojunction perovskite solar cells via vapor-assisted solution process. *J Am Chem Soc* 2014;136(2):622–5.
- Chen W, Wu Y, Liu J, Qin C, Yang X, Islam A, et al. Hybrid interfacial layer leads to solid performance improvement of inverted perovskite solar cells. *Energy Environ Sci* 2015;8(2):629–40.
- Zhou H, Chen Q, Li G, Luo S, Song T-b, Duan H-S, et al. Interface engineering of highly efficient perovskite solar cells. *Science* 2014;345(6196):542–6.
- Yang WS, Noh JH, Jeon NJ, Kim YC, Ryu S, Seo J, et al. High-performance photovoltaic perovskite layers fabricated through intramolecular exchange. *Science* 2015;348(6240):1234–7.
- Saliba M, Matsui T, Seo J-Y, Domanski K, Correa-Baena J-P, Nazeeruddin MK, et al. Cesium-containing triple cation perovskite solar cells: improved stability, reproducibility and high efficiency. *Energy Environ Sci* 2016;9(6):1989–97.

- [52] Saliba M, Matsui T, Domanski K, Seo J-Y, Ummadisingu A, Zakeeruddin SM, et al. Incorporation of rubidium cations into perovskite solar cells improves photovoltaic performance. *Science* 2016;354(6309):206–9.
- [53] Zhu Z, Bai Y, Liu X, Chueh CC, Yang S, Jen AKY. Enhanced efficiency and stability of inverted perovskite solar cells using highly crystalline SnO₂ nanocrystals as the robust electron-transporting layer. *Adv Mater* 2016;28(30):6478–84.
- [54] You J, Meng L, Song T-B, Guo T-F, Yang YM, Chang W-H, et al. Improved air stability of perovskite solar cells via solution-processed metal oxide transport layers. *Nat Nanotechnol* 2016;11(1):75–81.
- [55] Ye S, Sun W, Li Y, Yan W, Peng H, Bian Z, et al. CuSCN-based inverted planar perovskite solar cell with an average PCE of 15.6%. *Nano Lett* 2015;15(6):3723–8.
- [56] Kim JH, Liang PW, Williams ST, Cho N, Chueh CC, Glaz MS, et al. High-performance and environmentally stable planar heterojunction perovskite solar cells based on a solution-processed copper-doped nickel oxide hole-transporting layer. *Adv Mater* 2015;27(4):695–701.
- [57] Kim H-S, Lee C-R, Im J-H, Lee K-B, Moehl T, Marchioro A, et al. Lead iodide perovskite sensitized all-solid-state submicron thin film mesoscopic solar cell with efficiency exceeding 9%. *Sci Rep* 2012;2:591.
- [58] Chen W, Wu Y, Yue Y, Liu J, Zhang W, Yang X, et al. Efficient and stable large-area perovskite solar cells with inorganic charge extraction layers. *Science* 2015;350(6263):944–8.
- [59] Heo JH, Han HJ, Kim D, Ahn TK, Im SH. Hysteresis-less inverted CH₃ NH₃ PbI₃ planar perovskite hybrid solar cells with 18.1% power conversion efficiency. *Energy Environ Sci* 2015;8(5):1602–8.
- [60] Wu Y, Yang X, Chen W, Yue Y, Cai M, Xie F, et al. Perovskite solar cells with 18.21% efficiency and area over 1 cm² fabricated by heterojunction engineering. *Nat Energy* 2016;1:16148.
- [61] Li X, Bi D, Yi C, Décoppet J-D, Luo J, Zakeeruddin SM, et al. A vacuum flash-assisted solution process for high-efficiency large-area perovskite solar cells. *Science* 2016;aaf8060.
- [62] Kitazawa N, Watanabe Y, Nakamura Y. Optical properties of CH₃NH₃PbX₃ (X = halogen) and their mixed-halide crystals. *J Mater Sci* 2002;37(17):3585–7.
- [63] Ahmadian-Yazdi MR, Zabih F, Habibi M, Eslamian M. Effects of process parameters on the characteristics of mixed-halide perovskite solar cells fabricated by one-step and two-step sequential coating. *Nanoscale Res Lett* 2016;11(1):408.
- [64] Noel NK, Stranks SD, Abate A, Wehrenfennig C, Guarnera S, Haghighirad A-A, et al. Lead-free organic–inorganic tin halide perovskites for photovoltaic applications. *Energy Environ Sci* 2014;7(9):3061–8.
- [65] Eperon GE, Burlakov VM, Docampo P, Goriely A, Snaith HJ. Morphological control for high performance, solution-processed planar heterojunction perovskite solar cells. *Adv Funct Mater* 2014;24(1):151–7.
- [66] Park N-G. Methodologies for high efficiency perovskite solar cells. *Nano Converg* 2016;3(1):1–13.
- [67] Steitz R, Jaeger W, Klitzing Rv. Influence of charge density and ionic strength on the multilayer formation of strong polyelectrolytes. *Langmuir* 2001;17(15):4471–4.
- [68] Im J-H, Kim H-S, Park N-G. Morphology-photovoltaic property correlation in perovskite solar cells: one-step versus two-step deposition of CH₃NH₃PbI₃. *Appl Mater* 2014;2(8):081510.
- [69] Son D-Y, Lee J-W, Choi YJ, Jang I-H, Lee S, Yoo PJ, et al. Self-formed grain boundary healing layer for highly efficient CH₃ NH₃ PbI₃ perovskite solar cells. *Nat Energy* 2016;1:16081.
- [70] Xiao M, Huang F, Huang W, Dkhissi Y, Zhu Y, Etheridge J, et al. A fast deposition-crystallization procedure for highly efficient lead iodide perovskite thin-film solar cells. *Angew Chem* 2014;126(37):10056–61.
- [71] Wang L-Y, Deng L-L, Wang X, Wang T, Liu H-R, Dai S-M, et al. Di-isopropyl ether assisted crystallization of organic–inorganic perovskites for efficient and reproducible perovskite solar cells. *Nanoscale* 2017;9(45):17893–901.
- [72] Konstantakou M, Perganti D, Falaras P, Stergiopoulos T. Anti-solvent crystallization strategies for highly efficient perovskite solar cells. *Crystals* 2017;7(10):291.
- [73] Li T, Pan Y, Wang Z, Xia Y, Chen Y, Huang W. Additive engineering for highly efficient organic–inorganic halide perovskite solar cells: recent advances and perspectives. *J Mater Chem A* 2017;5(25):12602–52.
- [74] Chang C-Y, Chu C-Y, Huang Y-C, Huang C-W, Chang S-Y, Chen C-A, et al. Tuning perovskite morphology by polymer additive for high efficiency solar cell. *ACS Appl Mater Interfaces* 2015;7(8):4955–61.
- [75] Zhao Y, Wei J, Li H, Yan Y, Zhou W, Yu D, et al. A polymer scaffold for self-healing perovskite solar cells. *Nat Commun* 2016;7:10228.
- [76] Tripathi N, Shirai Y, Yanagida M, Karen A, Miyano K. Novel surface passivation technique for low-temperature solution-processed perovskite PV cells. *ACS Appl Mater Interfaces* 2016;8(7):4644–50.
- [77] Guo Y, Shoyama K, Sato W, Nakamura E. Polymer stabilization of lead (II) perovskite cubic nanocrystals for semitransparent solar cells. *Adv Energy Mater* 2016;6:6.
- [78] Wang Y, Luo J, Nie R, Deng X. Planar perovskite solar cells using CH₃NH₃PbI₃ films: a simple process suitable for large-scale production. *Energy Technol* 2016;4(4):473–8.
- [79] Abdi-Jalebi M, Dar MI, Sadhana A, Senanayak SP, Franckevičius M, Arora N, et al. Impact of monovalent cation halide additives on the structural and optoelectronic properties of CH₃NH₃PbI₃ perovskite. *Adv Energy Mater* 2016;6:10.
- [80] Boopathi KM, Mohan R, Huang T-Y, Budiawan W, Lin M-Y, Lee C-H, et al. Synergistic improvements in stability and performance of lead iodide perovskite solar cells incorporating salt additives. *J Mater Chem A* 2016;4(5):1591–7.
- [81] Wu Y, Xie F, Chen H, Yang X, Su H, Cai M, et al. Thermally stable MAPbI₃ perovskite solar cells with efficiency of 19.19% and area over 1 cm² achieved by additive engineering. *Adv Mater* 2017;29(28).
- [82] Zhang T, Yang M, Zhao Y, Zhu K. Controllable sequential deposition of planar CH₃NH₃PbI₃ perovskite films via adjustable volume expansion. *Nano Lett* 2015;15(6):3959–63.
- [83] Liang PW, Liao CY, Chueh CC, Zuo F, Williams ST, Xin XK, et al. Additive enhanced crystallization of solution-processed perovskite for highly efficient planar-heterojunction solar cells. *Adv Mater* 2014;26(22):3748–54.
- [84] Xiao Z, Bi C, Shao Y, Dong Q, Wang Q, Yuan Y, et al. Efficient, high yield perovskite photovoltaic devices grown by interdiffusion of solution-processed precursor stacking layers. *Energy Environ Sci* 2014;7(8):2619–23.
- [85] Emslie AG, Bonner FT, Peck LG. Flow of a viscous liquid on a rotating disk. *J Appl Phys* 1958;29(5):858–62.
- [86] Wu Y, Islam A, Yang X, Qin C, Liu J, Zhang K, et al. Retarding the crystallization of PbI₂ for highly reproducible planar-structured perovskite solar cells via sequential deposition. *Energy Environ Sci* 2014;7(9):2934–8.
- [87] Im J-H, Jang I-H, Pellet N, Grätzel M, Park N-G. Growth of CH₃NH₃PbI₃ cuboids with controlled size for high-efficiency perovskite solar cells. *Nat Nanotechnol* 2014;9(11):927–32.
- [88] Zheng E, Wang X-F, Song J, Yan L, Tian W, Miyasaka T. PbI₂-based dipping-controlled material conversion for compact layer free perovskite solar cells. *ACS Appl Mater Interfaces* 2015;7(32):18156–62.
- [89] Liu T, Hu Q, Wu J, Chen K, Zhao L, Liu F, et al. Mesoporous PbI₂ scaffold for high-performance planar heterojunction perovskite solar cells. *Adv Energy Mater* 2016;6:3.
- [90] Ko H, Sin DH, Kim M, Cho K. Predicting the morphology of perovskite thin films produced by sequential deposition method: a crystal growth dynamics study. *Chem Mater* 2017;29(3):1165–74.
- [91] Liang K, Mitzi DB, Prikas MT. Synthesis and characterization of organic–inorganic perovskite thin films prepared using a versatile two-step dipping technique. *Chem Mater* 1998;10(1):403–11.
- [92] Shi J, Luo Y, Wei H, Luo J, Dong J, Lv S, et al. Modified two-step deposition method for high-efficiency TiO₂/CH₃NH₃PbI₃ heterojunction solar cells. *ACS Appl Mater Interfaces* 2014;6(12):9711–8.
- [93] Chen Q, Zhou H, Hong Z, Luo S, Duan H-S, Wang H-H, et al. Planar heterojunction perovskite solar cells via vapor-assisted solution process. *J Am Chem Soc* 2013;136(2):622–5.
- [94] Mariano F, Listorti A, Rizzo A, Colella S, Gigli G, Mazzeo M. Thermally evaporated hybrid perovskite for hetero-structured green light-emitting diodes. *Appl Phys Lett* 2017;111(16):163301.
- [95] Yu JC, Kim DW, Kim DB, Jung ED, Park JH, Lee AY, et al. Improving the stability and performance of perovskite light-emitting diodes by thermal annealing treatment. *Adv Mater* 2016;28(32):6906–13.
- [96] Ting J-M, Huang N. Thickening of chemical vapor deposited carbon fiber. *Carbon* 2001;39(6):835–9.
- [97] Jensen KF, Graves D. Modeling and analysis of low pressure CVD reactors. *J Electrochem Soc* 1983;130(9):1950–7.
- [98] Jones APO' Brien. CVD of compound semiconductors. Weinheim: VCH; 1997.
- [99] Suresh A, Anastasio D, Burkey D, Michael Prof. L. Hitchman Dept. of pure and applied Chemistry University of Strathclyde 295 Cathedral street. *Chem Vap Depos* 2014;20(5):1–4.
- [100] Jones AC, Hitchman ML. Chemical vapour deposition: precursors, processes and applications. Royal Society of Chemistry; 2009.
- [101] Li Y, Mann D, Rolandi M, Kim W, Ural A, Hung S, et al. Preferential growth of semiconducting single-walled carbon nanotubes by a plasma enhanced CVD method. *Nano Lett* 2004;4(2):317–21.
- [102] Darr J, Guo Z, Raman V, Bououdina M, Rehman I. Metal organic chemical vapour deposition (MOCVD) of bone mineral like carbonated hydroxyapatite coatings. *Chem Commun* 2004;6:696–7.
- [103] Luo P, Liu Z, Xia W, Yuan C, Cheng J, Lu Y. Uniform, stable, and efficient planar-heterojunction perovskite solar cells by facile low-pressure chemical vapor deposition under fully open-air conditions. *ACS Appl Mater Interfaces* 2015;7(4):2708–14.
- [104] Leyden MR, Ono LK, Raga SR, Kato Y, Wang S, Qi Y. High performance perovskite solar cells by hybrid chemical vapor deposition. *J Mater Chem A* 2014;2(44):18742–5.
- [105] Yan X-T, Xu Y. Chemical vapour deposition: an integrated engineering design for advanced materials. Springer Science & Business Media; 2010.
- [106] Luo P, Zhou S, Xia W, Cheng J, Xu C, Lu Y. Chemical vapor deposition of perovskites for photovoltaic application. *Adv Mater Interfaces* 2017;4:8.
- [107] Eperon GE, Burlakov VM, Goriely A, Snaith HJ. Neutral color semitransparent microstructured perovskite solar cells. *ACS Nano* 2013;8(1):591–8.
- [108] Yin J, Qu H, Cao J, Tai H, Li J, Zheng N. Vapor-assisted crystallization control toward high performance perovskite photovoltaics with over 18% efficiency in the ambient atmosphere. *J Mater Chem A* 2016;4(34):13203–10.
- [109] Luo P, Liu Z, Xia W, Yuan C, Cheng J, Lu Y. A simple in situ tubular chemical vapor deposition processing of large-scale efficient perovskite solar cells and the research on their novel roll-over phenomenon in J–V curves. *J Mater Chem A* 2015;3(23):12443–51.
- [110] Chen CW, Kang HW, Hsiao SY, Yang PF, Chiang KM, Lin HW. Efficient and uniform planar-type perovskite solar cells by simple sequential vacuum deposition. *Adv Mater* 2014;26(38):6647–52.
- [111] Afzaal M, Salhi B, Al-Ahmed A, Yates H, Hakeem A. Surface-related properties of perovskite CH₃NH₃PbI₃ thin films by aerosol-assisted chemical vapour deposition. *J Mater Chem C* 2017;5(33):8366–70.
- [112] Chen S. Thin films deposition for energy efficient windows and solar cells. 2016.
- [113] Afzaal M, Yates HM. Growth patterns and properties of aerosol-assisted chemical

- vapor deposition of CH₃NH₃PbI₃ films in a single step. *Surf Coat Technol* 2017;321:336–40.
- [114] Bhachu D, Scanlon D, Saban E, Bronstein H, Parkin I, Carmalt C, et al. Scalable route to CH₃ NH₃ PbI₃ perovskite thin films by aerosol assisted chemical vapour deposition. *J Mater Chem A* 2015;3(17):9071–3.
- [115] Cao Q, Yang S, Gao Q, Lei L, Yu Y, Shao J, et al. Fast and controllable crystallization of perovskite films by microwave irradiation process. *ACS Appl Mater Interfaces* 2016;8(12):7854–61.
- [116] Ko CJ, Lin YK, Chen FC. Microwave annealing of polymer photovoltaic devices. *Adv Mater* 2007;19(21):3520–3.
- [117] Jung B, Kim K, Kim W. Microwave-assisted solvent vapor annealing to rapidly achieve enhanced performance of organic photovoltaics. *J Mater Chem A* 2014;2(36):15175–80.
- [118] Ahn N, Son D-Y, Jang I-H, Kang SM, Choi M, Park N-G. Highly reproducible perovskite solar cells with average efficiency of 18.3% and best efficiency of 19.7% fabricated via Lewis base adduct of lead (II) iodide. *J Am Chem Soc* 2015;137(27):8696–9.